Influence of timing cuts in Testbeam data and Simulation

Dissertation

zur Erlangung des Doktorgrades

des Department Physik

der Universität Hamburg

vorgelegt von

ELDWAN BRIANNE

aus Saint-Malo, Frankreich

Hamburg

2017

Gutachter/in der Dissertation:	Prof. Dr. Erika Garutti
	Dr. Katja Krüger
Gutachter/in der Disputation:	Dr. Jenny List
	????
Datum der Disputation:	????
Vorsitzender des Prüfungsausschusses:	????
Vorsitzender des Promotionsausschusses:	????
Dekan des Fachbereichs Physik:	????

Abstract

Etiam pede massa, dapibus vitae, rhoncus in, placerat posuere, odio. Vestibulum luctus commodo lacus. Morbi lacus dui, tempor sed, euismod eget, condimentum at, tortor. Phasellus aliquet odio ac lacus tempor faucibus. Praesent sed sem. Praesent iaculis. Cras rhoncus tellus sed justo ullamcorper sagittis. Donec quis orci. Sed ut tortor quis tellus euismod tincidunt. Suspendisse congue nisl eu elit. Aliquam tortor diam, tempus id, tristique eget, sodales vel, nulla. Praesent tellus mi, condimentum sed, viverra at, consectetuer quis, lectus. In auctor vehicula orci. Sed pede sapien, euismod in, suscipit in, pharetra placerat, metus. Vivamus commodo dui non odio. Donec et felis.

Zusammenfassung

Donec et nisl id sapien blandit mattis. Aenean dictum odio sit amet risus. Morbi purus. Nulla a est sit amet purus venenatis iaculis. Vivamus viverra purus vel magna. Donec in justo sed odio malesuada dapibus. Nunc ultrices aliquam nunc. Vivamus facilisis pellentesque velit. Nulla nunc velit, vulputate dapibus, vulputate id, mattis ac, justo. Nam mattis elit dapibus purus. Quisque enim risus, congue non, elementum ut, mattis quis, sem. Quisque elit.

Contents

Introduction

Chapter 1

Particle Physics: Theory

1.1   The Standard Model of Particle Physics

1.2   The Higgs Boson

1.3   Beyond the Standard Model

Chapter 2

The International Linear Collider: a future e^+e^- linear collider

2.1 Damping rings

2.2 Sources

2.3 Linac

2.4 ILC Physics

2.4.1 Higgs Physics

2.4.2 Electroweak Physics

2.4.3 Top mass measurement

2.4.4 Beyond the Standard Model

2.5 The International Large Detector (ILD)

Chapter 3

Calorimetery and Particle Flow Concept

3.1 Calorimetry in High Energy Physics

3.1.1 Particle interaction with matter

3.1.2 Calorimeters

3.2 Pandora, a Particle Flow Algorithm

Chapter 4

CALICE Calorimeter concepts

4.1 Electromagnetic Calorimeters

4.1.1 SiW-ECAL

4.1.2 Sc-ECAL

4.2 Hadronic Calorimeters

4.2.1 AHCAL

4.2.2 SDHCAL

4.2.3 DHCAL

Chapter 5

GEANT 4 Simulations

In High Energy Physics as well as in other reasearch area, simulations are a tool that has become indispensable. They are used to provide models predictions, a guideline for an analysis as well as for optimising cost and performance of detector designs. In this thesis, the simulations will be used as a guideline for the selection of specific events of the recorded data. An understanding of their functionning is useful and will be described in this chapter.

5.1 Simulation of particle showers

The GEANT 4 framework [1] is a common toolkit in particle physics to simulate particle interactions with matter for a wide range of energies. Within this thesis, the simulations of CALICE calorimeter prototypes and the ILD detector concept are used in conjunction with the MOKKA [2] and DD4HEP [3] framework. These frameworks provide a variety of tools for the implementation of detector geometries. GEANT 4 offers various tools and models to simulate physics processes in particle showers.

5.1.1 Electromagnetic showers

Electromagnetic showers are generally well understood. This is mainly due to the fact that electrons, positrons and photons are only involved and their interaction with matter is fairly simple as described in **??**. All EM interactions are simulated with a standard EM package in GEANT 4 [4]. This packages has been extensively compared to mainy observables measured in calorimeters to a level of $\leq 1\%$ [5].

Recently additions have been made to EM physics list with a _EMY suffix especially for ionisation processes in active medium. This is needed in order to correctly simulate thin

active layers where the detection method is very sensitive to the primary ionisation, like in gas detectors such as RPCs. The use of the _EMY physics list is greatly improving the agreement between data and simulation in the RPC based CALICE calorimeter prototype, the SDHCAL and DHCAL [6]. Many other suffix options are available depending on the type of physics, detector and precision needed for EM processes.

5.1.2 Hadronic showers

Hadronic showers are more complex in many ways than EM showers mainly due to the compositeness of the projectile as well as the target nuclei. High energy interaction between these lead to a very large phase space in the final state. This is governed by the strong force and typically the interaction cannot be solved analytically. Instead models are used using approximations and parametrisations mainly derived by theory and matched to data. Significant work has been made in the last few year in improving the modelisation and accuracy of such models. The CALICE Collaboration has been contributing extensively to these improvements [7, 8].

The scale of the interaction in hadronic showers is generally considered by the variable $\lambda_B = \frac{h}{p}$ called the De Broglie wavelength. This simple variable become shorter as the particle energy increases thus smaller structures inside a nuclei become more relevant for the description of the interaction. GEANT 4 provides several cascade models that are valid over various energy ranges. These models are described in the following.

5.1.2.1 Intra-Nuclear Cascade Models

For particle energies above few hundreds MeV and below few GeV, the quark substructure of the nuclei is irrelevant. In this case, the interaction can be described by cascade models (see figure 5.1). Several models are available in GEANT 4 and will be described in the following.

Bertini Cascade

The Bertini cascade model [10] consists of the modelisation of a nuclei by three concentric spherical shells of approximative constant nucleon density. The nucleons are treated as a degenerated Fermi gas in each shell and all energy levels are filled up until the Fermi energy (E_F). Following the Pauli exclusion principle, only nucleons of energy $E > E_F$ can interact in each region. During intra-nuclear-cascade (INC), the momentum, the type of
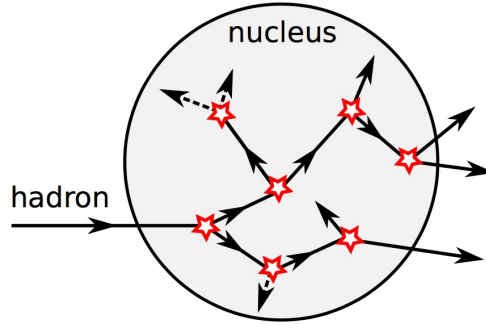
Figure 5.1 – Schematic of the cascade model. The incoming projectile and all secondaries inside the nuclei are tracked and their interaction is calculated until they are under a certain threshold or leave the nuclei. Taken from [9].

interaction and the four momentum of the interaction for each nucleon is calculated until the energy of the tracked nucleon is below 2 MeV. The INC gives rise to exited states of the nucleon, a pre-equlibrium evaporation as emission of protons and neutrons is computed. Then a de-excitation model is performed including Fermi break-up of highly excited light nuclei (A < 12), explosion model, fission model and evaporation model until the excitation energy is below 0.1 MeV.

Binary Cascade

The Binary cascade [11] is another approach to modelise the interaction between a projectile and a target nuclei. The model describes the nucleons with defined position and momentum following the nucleon mass, density distribution and Pauli's exclusion principle. The momentum is chosen randomly between zero and the Fermi momentum ($p_F^{max}(r)$) such as the total momentum of the nuclei is zero (at rest). The model is then treated by steps of excitations and decay into secondary particles emerging from the interaction until the average energy of all participants in the nuclei is below a given threshold (70 MeV). The remaining nuclei is further treated by pre-equilibrium and de-excitation models in GEANT 4. The validity range of this model extends from around 100 MeV up to 10 GeV.

5.1.2.2 String-Parton Cascade Models

The string-parton models [12] are used in GEANT 4 to simulate inelastic scattering of particles with a target nuclei as shown in figures 5.2a and 5.2b. This is used at energies where INC models break down and where the quark substructure of the nuclei must be
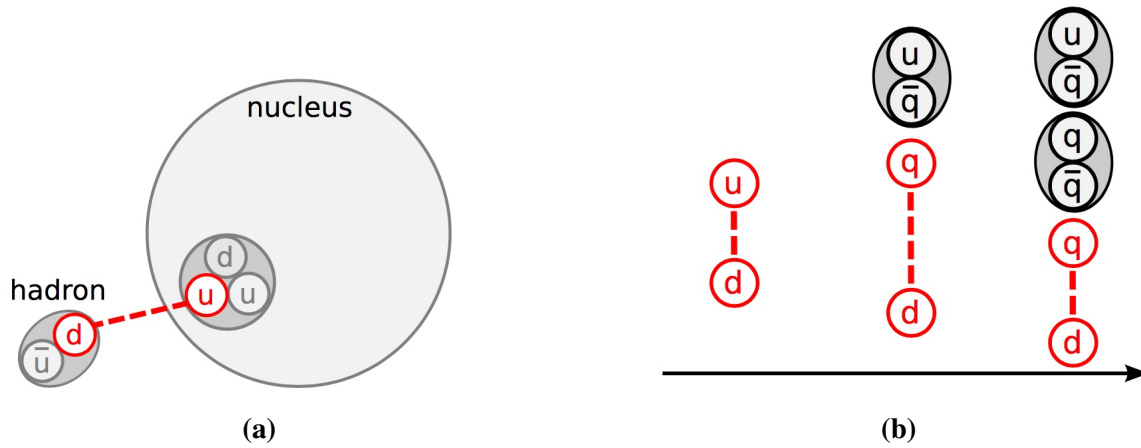
Figure 5.2 – a) The sketch shows the formation of a string between the projectile and one of the quarks inside the nuclei. b) Representation of the fragmentation of the strings via the generation of quarks-antiquarks pairs into hadrons. Taken from [9].

taken into account. The model uses string excitation to calculate the scaterring. Currently, GEANT 4 provides two different models, the Fritiof model (FTF) and the quark gluon string model (QGS). The latter will be described in the following.

The initial state consists of building the nuclei of individual protons and neutrons. The interaction between the primary particle and the nuclei gives place to one or more excited strings and a excited state nuclei. A string has two endpoints such as the quark content is defined and caries energy and momentum. The fragmentation of the strings is handled by a longitudinal string fragmentation model and the interaction of secondaries is carried out by cascade models as described in the former paragraph. The de-excitation is then simu-lated by fragmentation, pre-compound and nuclear de-excitation model natively provided by GEANT 4. The QGS model differs from the FTF model by the use of Pomerons as mediators for color exchange and momentum transfert.

5.1.3   GEANT 4 Physics Lists

GEANT 4 provides several physics lists for simulation that combines different hadron physics models. In this thesis, the physics lists QGSP_BERT and QBBC are used. The validity range of the physics list is shown in figure 5.3. The former is used in combinai-son with the High-Precision neutron tracking (HP) package. The HP option delivers an increased accuracy in the treatment of neutrons interactions below 20 MeV. The latter pos-sesses a comparable tracking for neutrons with less precision. In addition, the QGSP_BERT physics list uses a parametrised LEP model (based on expirimental data) to fill the gap be-
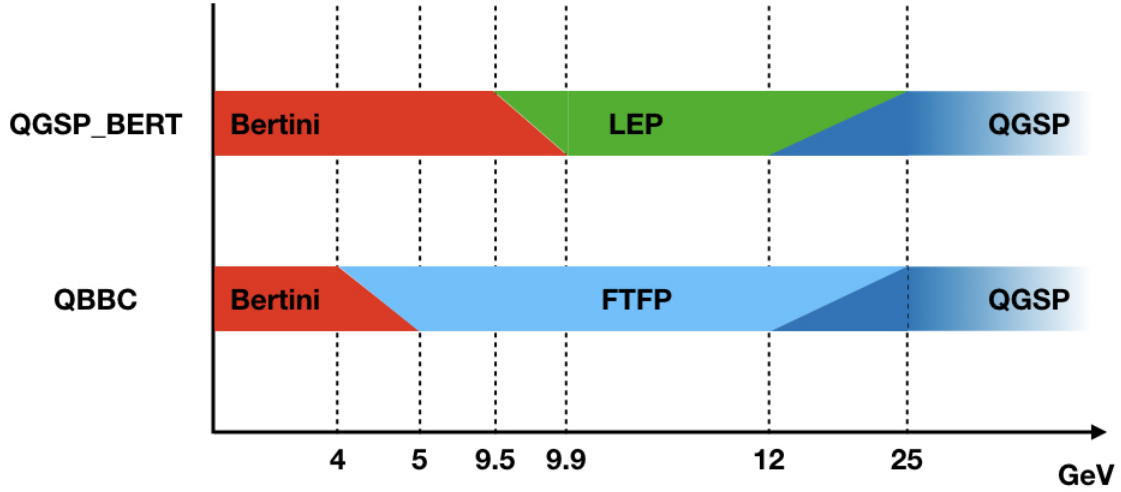
Figure 5.3 – Schematic of the physics list used in GEANT 4 for this thesis. The validity range extends over 30 GeV.

tween the transition of cascade models and string-parton models.

5.2 AHCAL Detector Geometry implementation and Digitisation

5.2.1 Geometry implementation

The simulation of the testbeam prototype is based on the MOKKA framework v08-05-01 and the new DD4HEP framework v00-16, which both provide a full GEANT 4 v10.1 based simulation of the detector implementations with detailed geometry and material descriptions. The right handed coordinate is used such as the Z-axis points in the beam direction and that the Y-axis is directed upwards. No beamline instrumentation is simulated except scintillator triggers in front and back of the detector. An additional layer of 5.6 mm of lead is added in front of the calorimeter in order to account for missing upstream material. This analysis uses the sub-detector MOKKA models *TBecal4d* for the ScECAL (Scintillator strips with EBUs) and *TBhcal4d* for the AHCAL. The distance between the sub-detectors is set to 0 mm. A check was performed between MOKKA and DD4HEP models with electrons and pions to ensure that the material description in both models are approximately the same.

The beam gun is placed 1 m in front of the calorimeter face for the simulations in this

analysis. It is configured to generate single beam particle with a 2% momentum spread (according to the beamline) and the beam profile for electrons and pions is extracted from data and applied to simulation. For muon runs, a flat beam covering the full AHCAL is simulated as this is not expected to have an influence on the MIP and time response of the detector. All electron simulations are simulated with GEANT 4 10.1 using the QGSP_BERT_HP physics list.

Pion showers are simulated using QGSP_BERT, QGSP_BERT_HP and QBBC physics lists. The package *high precision* (_HP) is used in order to understand the differences induced in timing with a precise treatment of the neutrons. For each energies, 100 000 simulated μ^-, e^- and 200 000 π^- single particle events are generated.

5.2.2 Digitisation

The digitisation of simulated hits is very similar to the one used in the ScECAL and AHCAL physics prototypes [13]. Using, if available, individual calibration factors obtained from data to extract the light yield which is needed to model the statistical fluctuations of photons hitting a SiPM. Saturation effects are also included using the number of pixels available on each SiPM type. Most of the tiles used are wrapped with a reflective foil in order that crosstalk effect between channels can be neglected. For layers with no wrapping a default value of 15% cross-talk is applied. The timing is modelled in the same way as in the SPIROC, the energy from sub-hits in a cell is integrated over a sliding time window of 15 ns, if the energy sum passes the threshold the time of the simulated sub-hit passing the threshold is registered as the time of the hit.

In order to simulate detector resolution effects, the time of a hit is smeared with a double gaussian function with slightly different means and sigmas convoluted with a gaussian of fixed mean and variable sigma. More details are explained in appendix **??**. Noise needs to be taken into account for with the engineering AHCAL prototype. Noise is added using muon runs by removing found tracks and keeping remaining hits. This is described in appendix **??**.

After digitisation, simulated hits have the same format as raw data hits and are then reconstructed using the same software chain used for data. To suppress noise, only hits above 0.5 MIP are considered in this analysis in both simulation and data.

Chapter 6

Commissioning of the AHCAL

6.1   Commissioning procedure

6.2   Noise Measurement in the AHCAL

Chapter 7

Energy Calibration of the AHCAL

7.1 Beamline Setup

7.2 TestBeam Setup

7.3 Energy Calibration of the AHCAL

Chapter 8

Timing study of hadronic showers in the AHCAL technological prototype

The International Large Detector (ILD) as mentionned in **??** considers a highly granular hadronic calorimeter using iron absorbers to achieve a compact detector with the best jet energy resolution around 3-4% at 250 GeV satisfying the space constrain imposed by the solenoid magnet. Timing measurements in a calorimeter can be used to reject pile-up events like at the LHC or CLIC due to the bunch-to-bunch spacing of 25 and 0.5 ns respectively. Also the high level of $\gamma\gamma \rightarrow$ hadrons could be rejected by using timing information of the calorimeter in order to limit the impact of the background on physics measurements. Novel techniques of using time information to improve energy reconstruction could be used [14].

In the hadronic calorimeter, the timing precision is highly influenced by the time structure of the shower itself. A hadronic shower possesses several timing components related to different processes happening in the shower. A fast component related to instantaneous highly energetic deposits from high-energy hadrons and electromagnetic sub-showers. A slow component due to neutron scattering, nuclear-recoil and photons from nuclear processes, this component can last up to several milliseconds. Apart from physics processes, the measured hit time is influenced by the active medium used as well as the electronics. Time constants in the active medium such as scintillation decay time can affect the measurement.

The performance of the ILD relies on simulation studies based on GEANT 4, it is important to study how well the simulation performs to reproduce the time structure of hadronic showers observed in data. The CALICE Analog Hadronic Calorimeter (AHCAL) techno-

Table 8.1 – List of channels with the injected trigger signal to be used as time reference.

Layer #	Chip Number	Channel	Comments	Appellation
11	169	29	noisy	T_{11}
11	177	23	broken	-
12	185	29	-	T_{12}
13	201	29	-	T_{13}
13	211	6	broken	-
14	217	23	-	T_{14}

logical prototype has been installed in the SPS CERN facilities in July and August 2015 in order to provide measurements using plastic scintillators. The goal of this study is to improve our knowledge about hadronic showers especially about its time evolution and time correlations of layers within the calorimeter. This note will describe the timing calibration procedure of the AHCAL first, the comparison with simulation for muons and electrons and finally a comparison with pion data.

8.1   Runs & Event Selection

8.1.1   Trigger Signals

For a muon beam, two scintillator plates of 50×50 cm^2 were placed in front and back of the calorimeter. For electron and pion beams, two small scintillator plates of 10×10 cm^2 were positioned in front of the calorimeter. The trigger scintillators were connected to a NIM-logic (discriminator and gate) in order to provide a validation of the data to the chip. In order to provide the time reference of the triggers, a SiPM-like pulse of around 4 μs length and with a fast rising edge around 1 ns was generated from the NIM-logic. This signal was injected directly via AC coupling to some channels in the setup as shown in the table 8.1. No other external time reference than these channels is available. In the following analysis, only the reference signals T_{12}, T_{13} and T_{14} were used.

8.1.2   Dataset

During the campaign at SPS in July 2015, μ^- runs were taken at 50 and 150 GeV beam energy for the calibration of the detector. Several e$^-$ runs were taken between 10 to 50 GeV beam energy to study the electromagnetic response of the calorimeter. The e$^-$ runs were quite pure as the beam was generated via a neutral beam directed on a converter target. Due

Table 8.2 – List of runs taken at SPS in July 2015.

Particle	Energy	Runs
μ^-	50 GeV	24016-24204
	150 GeV	24623-24662
e^-	10 GeV	24531-24576
	15 GeV	24507-24527
	20 GeV	24479-24504
	30 GeV	24454-24475
	40 GeV	24420-24448
	50 GeV	24404-24419
π^-	10 GeV	24266-24272, 24300-24317, 24381-24397
	20 GeV	24398-24400
	30 GeV	24259-24299, 24319-24380
	50 GeV	24212-24254, 24325-24357, 24580-24612
	70 GeV	24219-24242, 24365-24374
	90 GeV	24233-24287, 24331-24364

to the significant amount of air and beam line instrumentation between the calorimeter and the final momentum selection magnet as well as few information of the beam parameters, the beam profile of electron runs is not well reproduced in simulation. Finally, π^- runs were taken between 10 to 90 GeV beam energy. The table 8.2 sums up the dataset taken.

8.1.3   Muon Selection

The μ runs were taken first at 50 GeV then another scan at the end of the campaign was performed at 150 GeV. The muon beam was produced by scrapping the halo of a secondary pion beam using collimators. The muon runs were contaminated by pions, a first estimation provided that around 30% of the events were contaminated. The main goal of the muon selection was to efficiently select muons and reject pion showers. For this, a simple track finder has been developed. In order to select muons or punch-through pions, a straight track of at least 7 hits is required in the whole AHCAL without a hard interaction. In addition to reject late pion showers, not more than 2 hits are required per layer.

8.1.4   Electron Selection

To perform comparisons on electron, a sample of events is selected from the data runs. A simple selection is performed in order to have mostly contained showers in the AHCAL. The selection cuts are summed up in table 8.4 for each energies.

Table 8.3 – Selection cuts for muon runs.

Name	Beam Energy	Cut
Preselection	All	$0 \text{ mm} < cog_z < 800 \text{ mm}$
	All	$0 < n_{hits} < 20$
Track Selection SSF	All	n_{hits} in tower > 7
	All	n_{hits} in layer < 3
Track Selection BL	All	n_{hits} in tower > 2
	All	n_{hits} in layer < 3

Table 8.4 – Selection cuts for each electron energies.

Name	Beam Energy	Cut
Event Quality	All	Cherenkow ON
	All	Energy in the first 3 layers of AHCAL > 10 MIP
Electron Selection	10 GeV	$25 < n_{hits} < 75$
	15 GeV	$30 < n_{hits} < 90$
	20 GeV	$40 < n_{hits} < 100$
	30 GeV	$50 < n_{hits} < 110$
	40 GeV	$60 < n_{hits} < 120$
	50 GeV	$70 < n_{hits} < 140$
	All	$cog_z < 250 \text{ mm}$
	All	$-90 \text{ mm} < cog_{x,y} < 90 \text{ mm}$
	All	Energy in last two layers $< 1\% \, E_{sum}$

8.1.5   Pion Selection

A simple selection is performed on pion events. The goal is to reject punch-through pions, muons and electron contamination. The selection cuts are shown in table 8.5.

8.2   Timing Calibration

To perform the timing calibration of the AHCAL, the complete muon dataset is used. The electron dataset is used in a next step to validate the calibration procedure as described in subsection 8.2.4. Table 8.6 summarises the runs and datasets used. Raw events are considered if the reference signals T_{12}, T_{13} and T_{14} are present in the event. Selected events are counted after the selection on the error of the time reference as explained in 8.2.2.1.

Table 8.5 – Selection cuts for pions.

Name	Beam Energy	Cut
Event Quality	All	Cherenkow OFF
Pion Selection	All	$n_{hits} > 20$
	All	n_{hits} in the first 2 AHCAL layers < 5
	All	Energy in last two layers > 1% E_{sum}

Table 8.6 – Table with the statistic before and after selection used for timing calibration.

| Runs	Energy	Particle Type	Events (Raw)	Events (sel.)	$\frac{N_{sel.}}{N_{raw}}$
24016-24663	50-150 GeV	μ^-	1851536	836796	45.2%
24528-24577	10 GeV	e^-	268275	216656	80.8%
24510-24520	15 GeV	e^-	108092	90395	83.6%
24486-24504	20 GeV	e^-	130232	110161	84.6%
24460-24470	30 GeV	e^-	82202	69692	84.8%
24427-24435	40 GeV	e^-	65901	55660	84.5%
24405-24419	50 GeV	e^-	123422	104030	84.3%

8.2.1 Slope calibration

The data analysis is performed in several steps. The first step is the calibration of the time provided by the SPIROC2B chip. To reconstruct the time of the first hit (only a single hit per channel is registered during a bunch-crossing) in a channel, the TDC value measured needs to be converted into nanoseconds. The value is converted using the following equations:

$$\text{slope}_{chip,BXID} \, [\text{ns/TDC}] = \frac{3920 \, \text{ns}}{\text{Max}_{chip,BXID} - \text{Pedestal}_{chip,BXID}} \tag{8.1}$$

$$\text{T}_{chn} \, [\text{ns}] = \text{slope}_{chip,BXID} \times (\text{TDC} - \text{Pedestal}_{mem=1}) \tag{8.2}$$

The determination of the parameter slope$_{chip,BXID}$ is assuming that the TDC ramp is linear. The parameters Max$_{chip,BXID}$ and Pedestal$_{chip,BXID}$ in eq.8.1 are extracted from the TDC spectrum from a specific chip and BXID using only the first memory cell as illustrated in figure 8.1a. At the same time, the parameter Pedestal$_{mem=1}$ in eq.8.2 is extracted from the spectrum for each channel and the first memory cell of a chip without taking into account the BXID of the ramp as the difference between both pedestal can be corrected for at a later stage. This is accounting for a total of 208 slopes and 3744 pedestals to be extracted for the testbeam setup.

The technique of extraction is based on an edge detection method. For each chip and
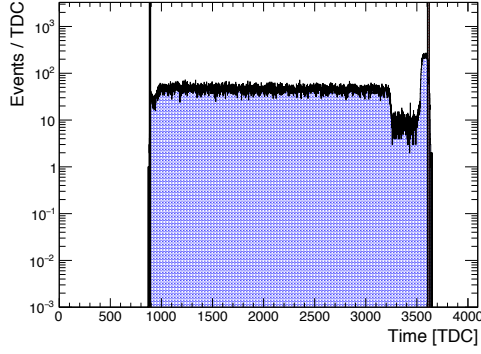
(a) TDC Spectrum of a typical chip.
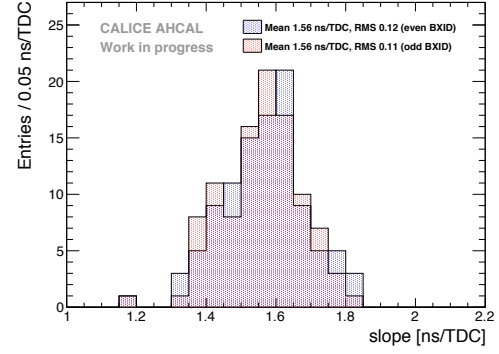
(b) Distribution of the fitted slopes for even and odd bunch-crossing IDs.

Figure 8.1 – a) The red rectangle are the fitted Max and Pedestal parameters for this chip. The yellow bands represents estimation of the error made on the extraction of the parameters by a variation of 1 RMS of the threshold μ. The parameters extracted are slope = 1.56 $\pm$ 0.01, Pedestal = 816 $\pm$ 9 and Maximum = 3336 $\pm$ 8. b) Tμ_{odd} = 1.564 ns/TDC, RMS$_{odd}$ = 0.121, μ_{even} = 1.556 ns/TDC, RMS$_{even}$ = 0.113.

BXID, an histogram is filled with the y value of each bin then the mean of this histogram is defined as a threshold μ. The parameter Pedestal$_{chip,BXID}$ is extracted as the first bin above 30% of μ. For the parameter Max$_{chip,BXID}$, it is extracted by taking 50% of the maximum bin of the original histogram. The maximum seems not to be exactly at the last bin of the spectrum, this is due to the technique that needed to be robust against strange spectra. An estimation of the errors made on the pedestal and maximum is done by looking at the maximum difference between 1 RMS of μ and 33% of the maximum bin to the extracted value. More details about the estimations of the calibration errors is described in the appendix **??**. The extracted values for the slopes are in the expected range of 1.6 ns per TDC bin due to the limited dynamic range provided by the chip (around 2500 bins for 4 μs) which is in aggreement with figure 8.1b.

8.2.2   Determination of the time of first hit

8.2.2.1   Time reference

To reconstruct the time of the first hit in a channel, the measured time of a hit needs to be compared to the time of the reference trigger. The trigger signals described in subsection 8.1.1 are calibrated using the same method as explained above. After time calibration of the hit, events are selected by requiring that T$_{12}$, T$_{13}$ and T$_{14}$ are present in the event in a certain amplitude range to reject noise hits from theses channels. In addition, as these channels
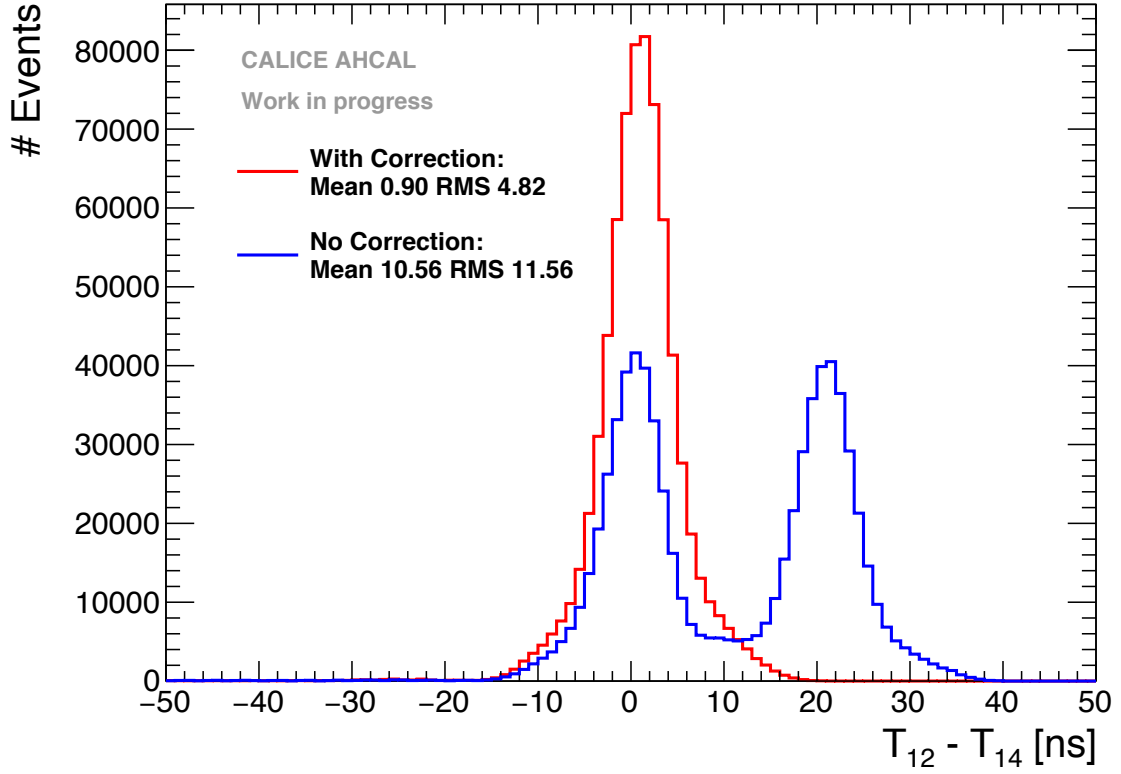
Figure 8.2 – Time difference between the trigger channels before and after correction for T_{12} and T_{14}. The histogram in blue shows the difference between the channels before correction, the histogram in red shows the difference after correction. $\mu = 10.6$ ns, RMS = 11.6 ns, $\mu_{corrected} = 0.9$ ns, RMS$_{corrected} = 4.8$ ns

receive exactly the same signal from the NIM-logic at the same time, a quadratic correction is applied to ensure that they match in time. The correction is performed by correcting the time of T_{12} and T_{13} compared to the time of T_{14}. The figure 8.2 shows that the correction reduces the spread of the trigger channels w.r.t to each other. The resulting resolution for the reference trigger signal is around 4-5 ns, this resolution from the electronics contributes to the final timing resolution obtained.

In a next step, to reduce the uncertainty made on the time of the trigger, the time reference T_{ref} is calculated using the mean of T_{12}, T_{13} and T_{14} and its associated error σ_{ref} as shown in eq. 8.3 & 8.4. A cut of 4 ns is performed on σ_{ref} to reject events with a too large error on the time of the trigger.

$$T_{ref} = \frac{T_{12} + T_{13} + T_{14}}{3} \tag{8.3}$$
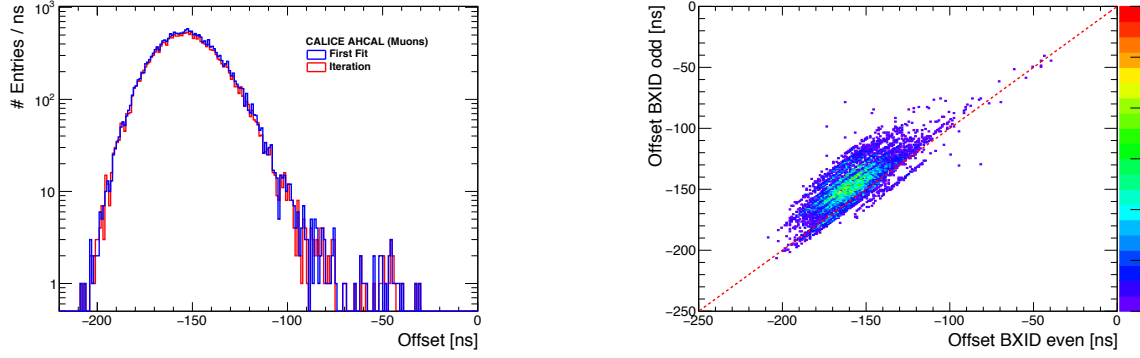
(a) Distribution of the offset used to correct for the trigger delay.

**(b)** Correlation between offsets extracted for even and odd BXID.

Figure 8.3 – a Extracted offset used to correct for the trigger delay signal. The mean delay of the trigger is ∼150 ns. b Correlation between offsets extracted for BXID even and odd.

$$\sigma_{ref}^2 = \frac{(T_{12} - T_{ref})^2 + (T_{13} - T_{ref})^2 + (T_{14} - T_{ref})^2}{6} \tag{8.4}$$

Since the absolute time between the passage of a muon and the trigger of a channel is not known due to cabling and the trigger electronics, the time offset relative to the trigger is determined from data. Muons are quasi-instantaneous particles thus the time of the first hit distribution for each channel, memory cells and BXID has to be shifted to $t=0$. This shifting procedure takes into account the delay time of the trigger due to cabling and the NIM-logic as well as mis-calibrations in pedestals. Only memory-cells containing more than 100 events are considered. This offset is determined by iteration requiring at least 4 prompt hits i.e hits in the range from -20 to 20 ns of the event. In this way, 18338 individual offsets are extracted from data. A distribution of the extracted offsets using muon data can be seen in figure 8.3a. The figure 8.3b shows that individual offsets have to be extracted for each BXID as the correlation is chip-dependent and not the same for odd and even BXIDs.

8.2.2.2   Time of the first hit distribution

After the selection, the time of the first hit (T_{fH}) can be obtained by plotting the distribution of T_{chn} - T_{ref} as shown in figure 8.4a. The combined time resolution (RMS) shown in figure 8.4b obtained by combining all layers is around 5.65 ns by just applying the time calibration on the data. Some improvements are possible as described in the subsections 8.2.3.1 and 8.2.3.2. The discrepancy observed for the layer 11 is most likely due to an electronic problem in the TDC voltage ramp of the chips on that layer.
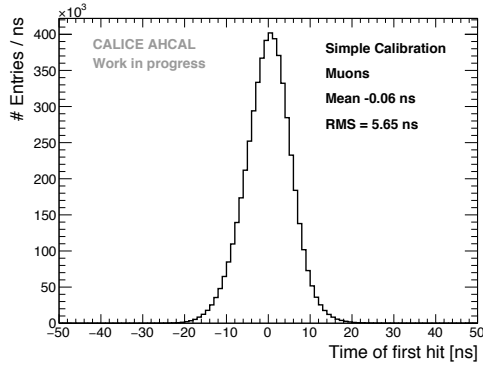
(a) Timing for all layers in the AHCAL.
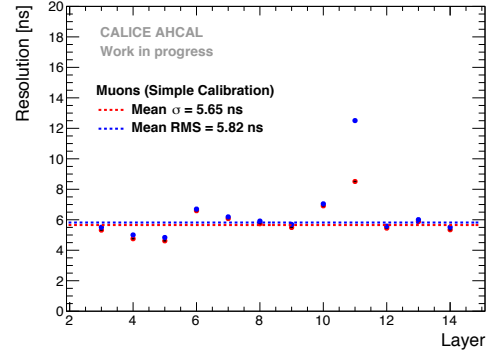
(b) Extracted resolution for all layers in the AHCAL.

Figure 8.4 – a Time of the first hit distribution of the AHCAL after the first part of the calibration. μ = -0.06 ns , RMS = 5.65 ns. The distribution is clearly asymmetric. b Time resolution for all layers in the AHCAL. The mean RMS is 5.65 ns.

8.2.3 Corrections applied to data

8.2.3.1 Ramp non-linearity correction

The calibration relies on the linearity of the TDC voltage ramp in the SPIROC2b by measuring the minimum and maximum of the ramp and interpolating assuming a linear ramp. This assumption is not entirely reliable as described in [**? ?**]. For this, a correction of the non-linearity has to be applied. By simply looking at the time of the first hit (T_{fH}) for each chip and BXID versus the TDC value of the hit, the shape of the graph would indicate how reliable is the assumption. Indeed if the ramp would be perfectly linear, one would obtain a flat graph. A quadratic fit is performed for each chip and BXID in order to correct for the non-linearity of the ramp as shown in figure 8.5a. A check has been performed on the quality of the correction, seen in figure 8.5b. The non-linearity correction results in an improvement on the timing resolution (RMS) of the AHCAL of ~5.1% (5.36 ns) as shown in figure 8.6a.

8.2.3.2 Time Walk correction

The time-walk effect is due to the presence of a threshold that induces a time shift between a small amplitude signal and a high amplitude signal. Small amplitude signals will systematically trigger at a later time than high amplitude signals. A correction can be applied on the data by looking at the time of the first hit versus the amplitude of the hit. This might be particularly important for late neutrons signals that generally deposit very
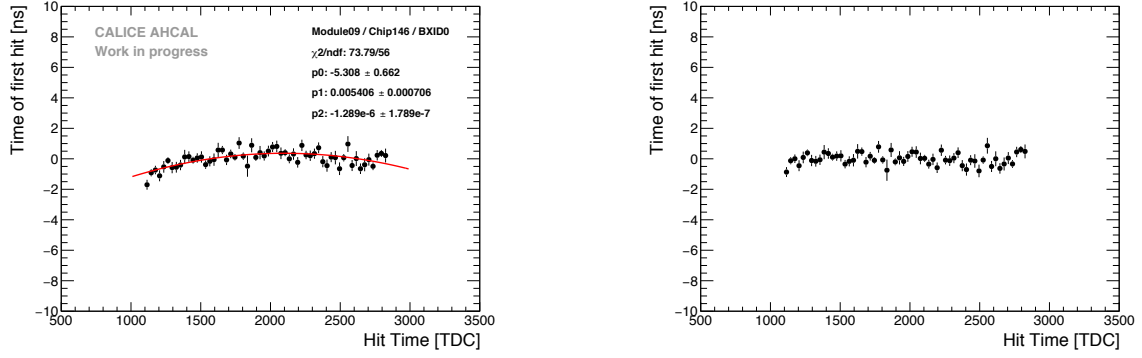
(a) Quadratic fit of chip 146 (BXID even) on layer 09.

(b) Profile for chip 146 on layer 09 after the non-linearity correction of the ramp.

Figure 8.5 – a The χ^2 of the fit is 1.29. b The correction parameter are applied then on the data to cross-check the quality of the correction. One can see that the curve flattens with the correction applied.

little energy in the calorimeter. The correction is assumed to be the same for all the chips, independent of the position of the threshold of each chip, as hits are cut at 0.5 MIP and most of the chips were having the threshold set-up well below 0.5 MIP. An exponential fit of the form $A \times e^{-\lambda x} + B$ is performed on the data to extract the parameters needed to correct the time walk effect as shown on figure 8.7a. The residuals after correction are in the order of few hundreds of picoseconds as seen in figure 8.7b.

8.2.3.3   Time of first hit for muons

After the time-walk correction, an improvement of $\sim$3% can be achieved on the time resolution of the AHCAL (RMS 5.20 ns) as shown in figure 8.8a. The figure 8.8b shows the time resolution obtained in the complete AHCAL. The obtained time resolution is around 5 ns. The distribution is still asymmetric, it is most likely coming from the non-linearity of the TDC ramp of the trigger reference as no external time is available to correct for it. This is taken into account in the simulation by parametrising the time distribution with a double Gaussian function. The number of events identified later than 5σ ($\sim$25 ns) is around 1.22% giving us a good assessment of the noise suppression for muons.

8.2.4   Cross-check of the calibration with electrons

In order to validate the calibration, an electron sample is taken. Electromagnetic showers are quasi-instantaneous and perfect to cross-check the time calibration procedure. The
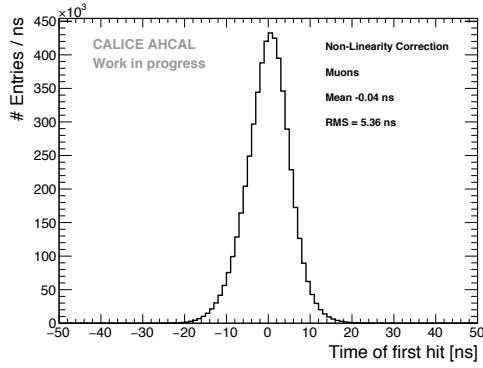
(a) Timing for all layers in the AHCAL.
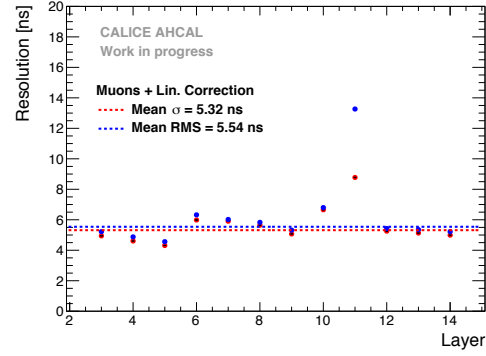
(b) Extracted resolution for all layers in the AHCAL.

Figure 8.6 – a Time of the first hit distribution of the AHCAL after the non-linearity correction. μ = -0.04 ns , RMS = 5.36 ns. b Time resolution for all layers in the AHCAL. The mean RMS is 5.54 ns.

selection applied to the data sample is described in subsection 8.1.4. The same calibration constants and correction constants are applied to the data except that an additional offset from the trigger signal has to be corrected for. The additional offset is expected to be small as the trigger configuration is very similar to the one for muons. The offset is in the order of 10 ns which is consistent with the changes in trigger configuration. The time of the first hit distribution is shown in figure 8.9. The time distribution presents a large tail to the right and is much wider than for muons. This gives a hint that an effect is present in electron data but not in muon data. The difference seen could be related to the fact that in electromagnetic showers, the number of hits is much higher as well as the energy deposited in a single cell can be over hundreds MIP.

8.2.5 Influence of the number of triggered channels

Pedestal shift for energy measurement is not a new feature of the SPIROC2b chip [?]. This electronic effect may be also present for timing measurement. It can be investigated by looking at the time of the first hit as a function of the number of triggered channels over 0.5 MIP. It is shown in figure 8.10a. This can be drastic on the time measurement of the AHCAL, a correction up to 15-20 ns can be necessary to the data for a high number of trigger. The correction parameters are determined by a linear fit to the data.
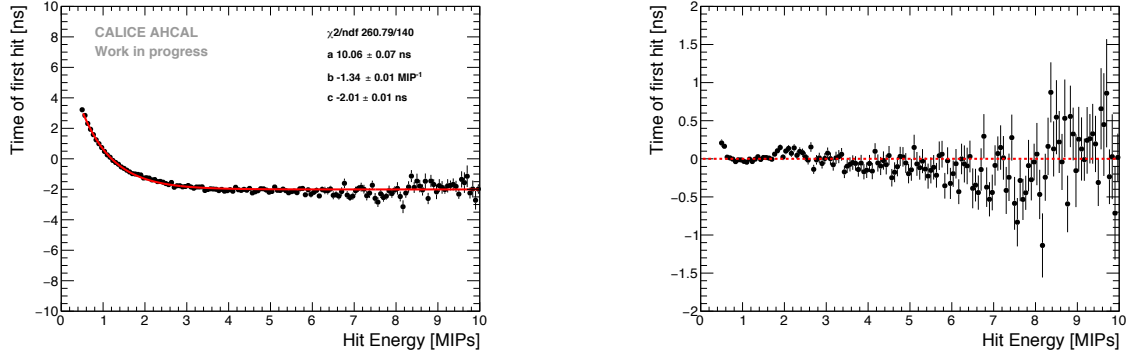
**(a)** Profile of the time of first hit as function of the hit energy.

(b) Same profile after time-walk correction.

Figure 8.7 – a Time-walk correction extracted from data. A = 10.06 $\pm$ 0.07, λ = -1.34 $\pm$ 0.01, B = -2.01 $\pm$ 0.01. A difference up to 6 ns is seen between small and large amplitudes. b Time-walk profile after correction showing a spread of less than 1 ns.

8.2.6 Time of the first hit for electrons

The distribution of the time of the first for 20 GeV is shown in figure 8.11a after correction. As seen the correction improves the RMS of the distribution ($\sim$14.6%) as well as the distribution appears more gaussian-like. However, there is still a discrepancy ($\sim$32.6%) with the time resolution obtained for muons (5 ns). This is due to the fact that not only the mean time shifts but that the RMS also increases as a function of number of hits as seen in figure 8.10b. In order for the simulation to match the data, the increase of the width of the time distribution has to be parametrised from the data. More details can be read in the appendix **??**. A comparison with the muon data has been done in order to cross-check the calibration as seen in figure 8.11b. If only single hits in a chip are taken, the time resolution obtained is very similar to the time resolution observed in muons ($\sim$7.7% difference).

The cause of observed effect is most likely due to an element in the chip (a delay box) that get unstable with the number of triggered channels and that is responsible for the hold of the TDC value in the chip. The hold is delayed thus sampling a higher TDC value than the one expected. All electron runs have been checked to validate the correction and calibration procedure. The figure 8.12 shows the comparison from 10 GeV to 50 GeV. The distributions are in agreement within a 10-15% range for all energies which is within systematical uncertainty as explained in subsection 8.2.7.
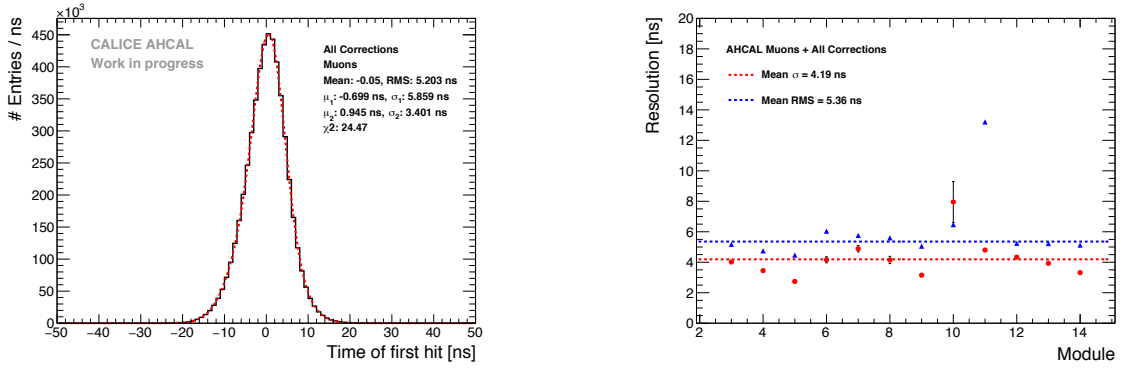
(a) Time of the first hit distribution of the AHCAL after all corrections.

(b) Time resolution obtained for each AHCAL layers.

Figure 8.8 – a Time of the first hit for muons after all corrections. b Time resolution obtained for each layer in the AHCAL. Mean RMS = 5.35 ns.

8.2.7   Influence of the detector inhomogeneity

A study has been performed to estimate the influence of the detector inhomogeneity on timing independent of the beam profile. For this, only events in which the centre of gravity in x and y are within the 4 centre tiles of the detector are selected. This has been checked for 10 and 50 GeV electron beam energy. The difference between the distribution can help to estimate the systematic uncertainty due to the inhomogeneity of the detector. The figures 8.13a and 8.13b show the time distribution for each tiles at 10 and 50 GeV respectively. The ratio shown is compared to the top left centre tile. One can see that for both energies, the distributions are within a 10-15% agreement. Therefore a conservative systematic uncertainty of 15% is assigned to electron and pion data in the following.

8.3   Comparison with simulation for muons and electrons

The next step is to compare data with simulation and cross-check the simulation with electrons. The timing resolution is extracted from muon data runs by fitting a double Gaussian in the range [-50 ns, 50 ns] and is used to smear the timing of simulated hits. The table 8.7 sums up the parameters used. The comparison for muons is shown in figure 8.14. The comparison shows that in the full range, the difference between data and simulation is around 10-20% maximum. This may be because of the asymmetry present in data that might be not well reproduced in Monte-Carlo. In general, the simulation is in a good agreement with data.
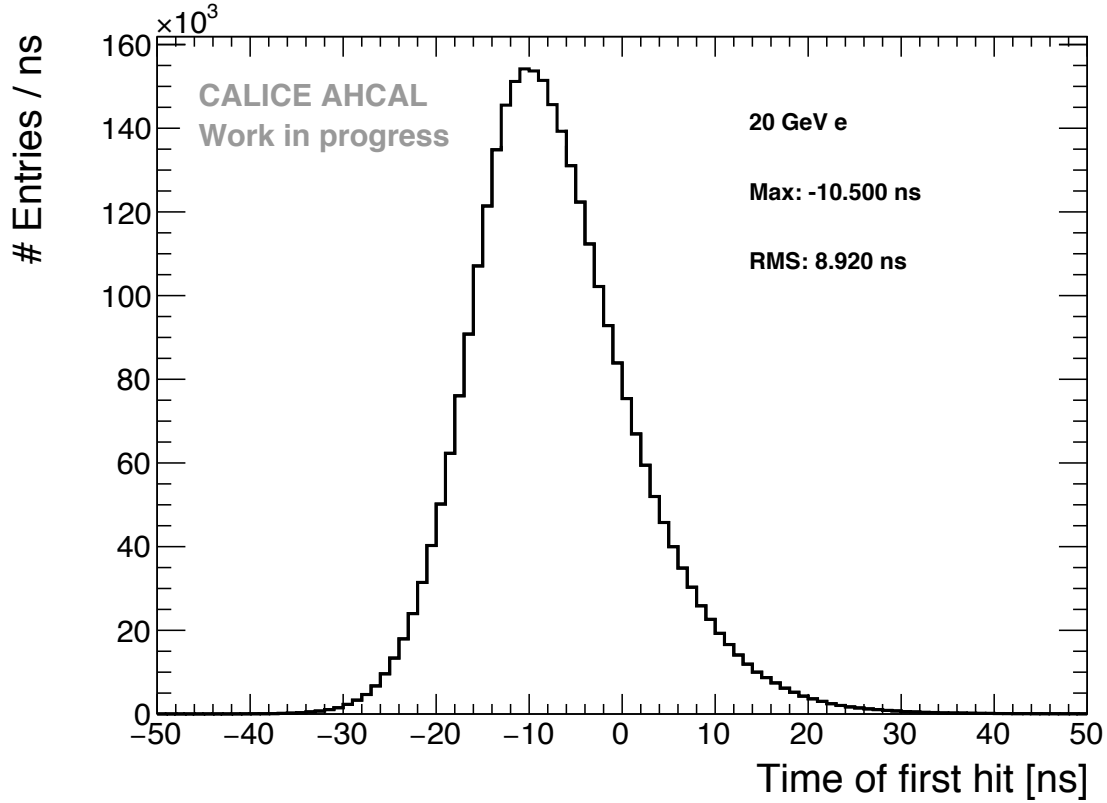
Figure 8.9 – Time of the first hit distribution for 20 GeV electrons, Max = 10.05 ns, RMS = 8.92 ns.

Table 8.7 – Timing resolution extracted with a double Gaussian fit from muon data used for simulation.[1]

μ_1 [ns]	σ_1 [ns]	μ_2 [ns]	σ_2 [ns]
-0.699095	5.8589	0.945278	3.40119

In the next step, a comparison with electron data is necessary to validate the simulation. In addition to the muon resolution, a parametrisation of the increase of the width of the time distribution function of the number of hits above 0.5 MIPs is added in simulation as described in appendix **??**. The figure 8.15 shows this comparison. The simulation is systematically narrower than data for all energies. This would suggest that simulation has less hits than data which is in agreement with figure 8.16, where generally simulation is 10-20% lower than data in the region of interest of 6 to 10 hits per chip. The simulation is in better agreement for higher energies (40-50 GeV) than for lower energies (10-15 GeV). This might come from the inhomogeneity of the detector that is not well reproduced in simulation by

---

[0]A table of rejected chips is available in appendix **??**.
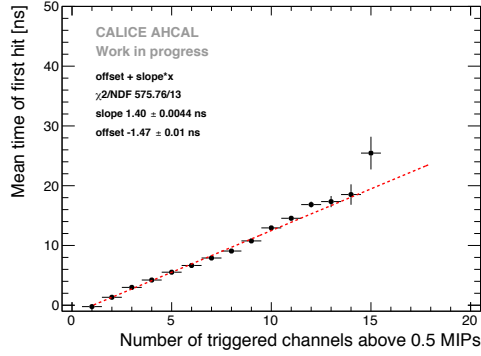
(a) Time of the first hit function of the number of triggered channels in a chip (20 GeV).
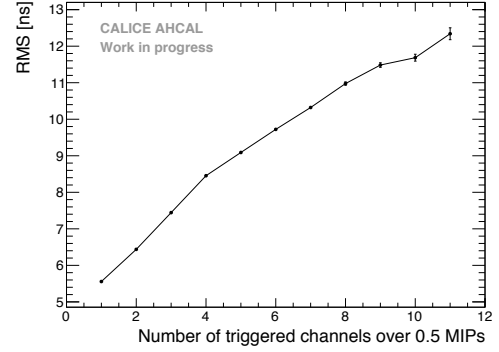
(b) RMS of the time of first hit function of the number of triggered channels (20 GeV).

Figure 8.10 – a The fit region is between 1 and 15 hits. A linear dependence is clearly visible. b The RMS of the time distribution can increase up to 12 ns for a high number of triggered channels.

the global time parametrisation used. This may suggest that the time parametrisation is chip-wise of layer-wise. But due to the limited amount of data, only a global time parametrisation can be applied. For 10 to 20 GeV comparisons, the description of the tails in simulation are quite underestimated. This may be due to the description of the noise in simulation that is not perfectly reproduced. Overall, the simulation and data are in agreement within uncertainties.
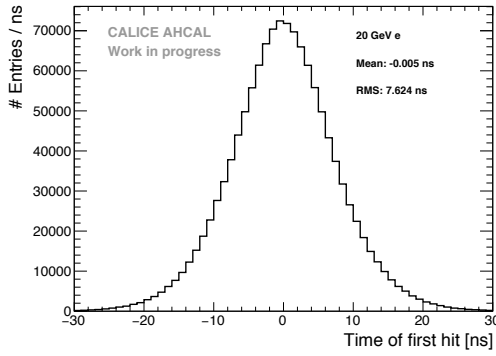
(a) Time of the first hit distribution for 20 GeV electrons after correction.
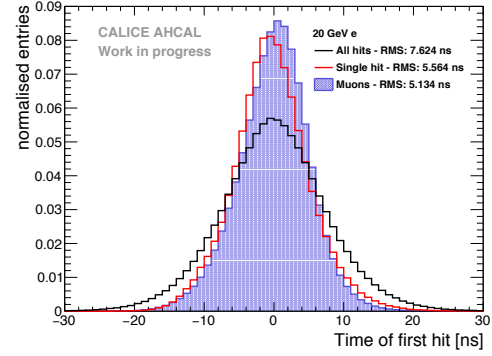
(b) Comparison with the muon time of first hit distribution.

Figure 8.11 – a Time of the first hit distribution for 20 GeV electrons after number of triggered channel correction, μ = -0.005 ns, RMS = 7.62 ns. b Comparison of the electron data sample, the time distribution is very similar to the muon one if only events with single hits in a chip are taken.

Table 8.8 – Table with the statistic before and after selection used for the pion dataset.

Runs	Energy	Particle Type	Events (3 T0s)	Events (sel.)	$\frac{N_{sel.}}{N_{raw}}$
24306-24317	10 GeV	π^-	425517	349012	82%
24381-24397					
24578-24612	50 GeV	π^-	1183790	1007889	85.1%
24339-24342	70 GeV	π^-	142813	122376	85.7%
24223-24238	90 GeV	π^-	466927	395884	84.8%
24273-24287					
24331-24336					
24358-24364					

8.4   Results

One of the main goal is to compared GEANT 4 simulation with different hadronic physics models to the recorded pion data. The table 8.8 summarises the runs and datasets used.

8.5   Summary
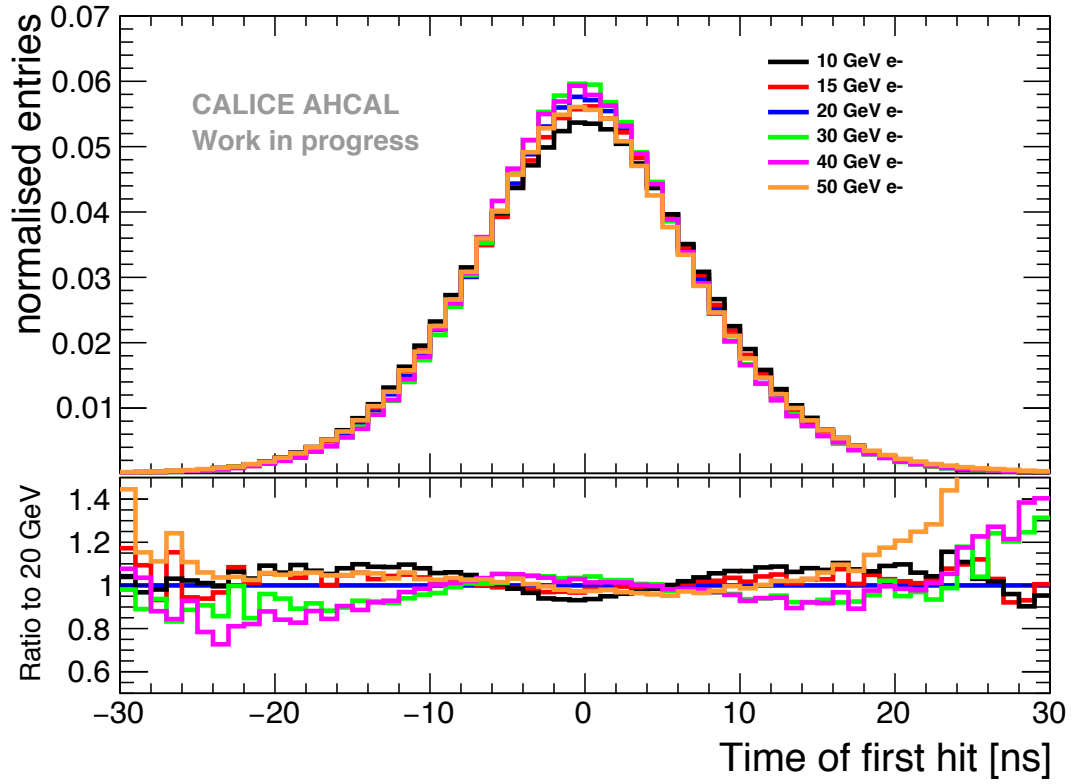
Figure 8.12 – Comparison of the time of first hit distribution for all electron energies.
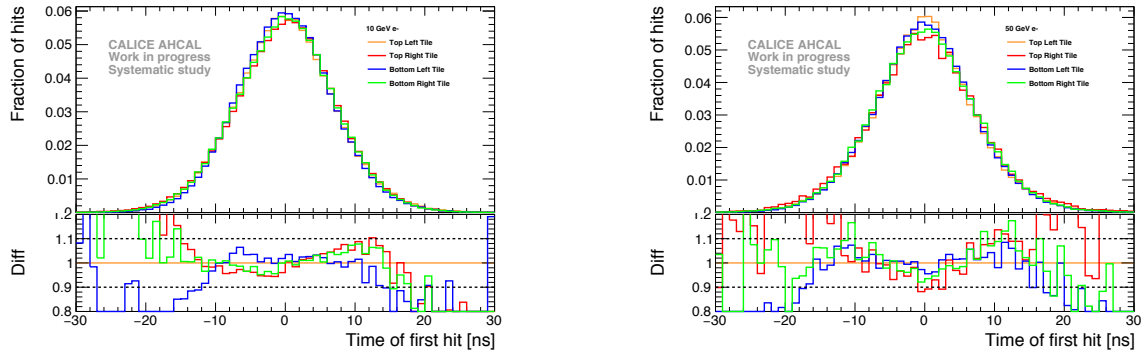
(a) Time of the first hit distribution at 10 GeV.

(b) Time of the first hit distribution at 50 GeV.

Figure 8.13 – a Time of the first hit distribution for all 4 tiles at 10 GeV. All distribution are within 10-15% in the core. b Time of the first hit distribution for all 4 tiles at 50 GeV. All distribution are within 10-15% in the core.
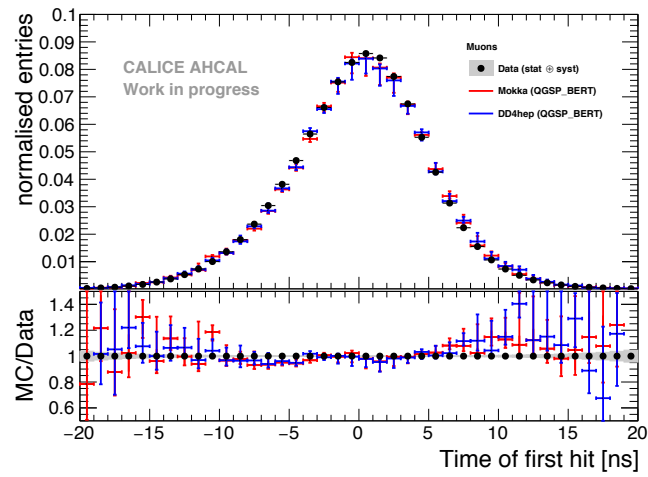
Figure 8.14 – Time of first hit for data and simulation between -20 and 20 ns.

(a) 10 GeV.

(b) 15 GeV.

(c) 20 GeV.

(d) 30 GeV.

(e) 40 GeV.

(f) 50 GeV.
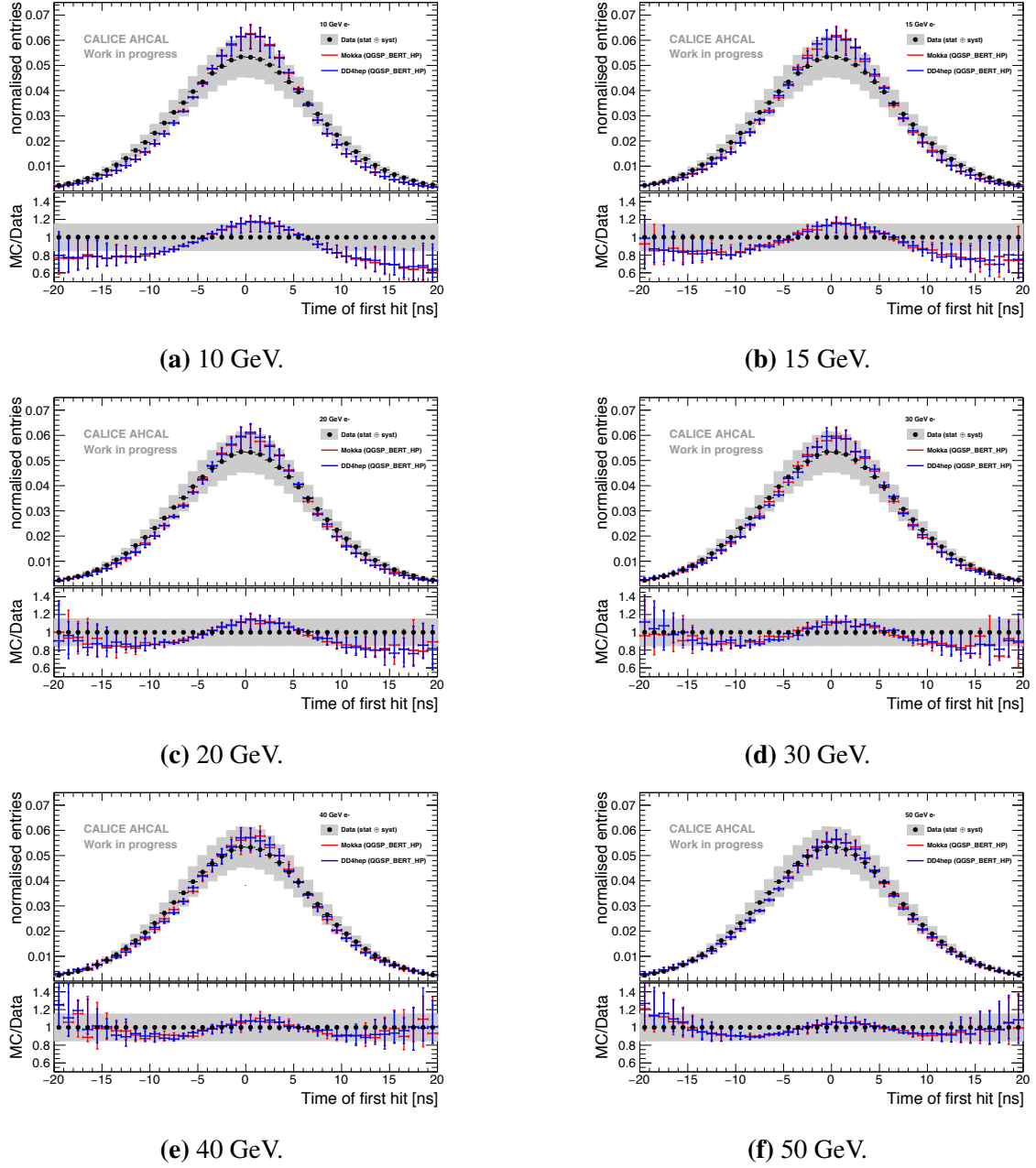
Figure 8.15 – Comparison between electron data and MC for all energies of the time of first hit. The grey area represents the statistical and systematical error of the data. Error bars in simulation are obtained by varying the cross-talk parameter and with the error envelope from the number of hits parameterisation.
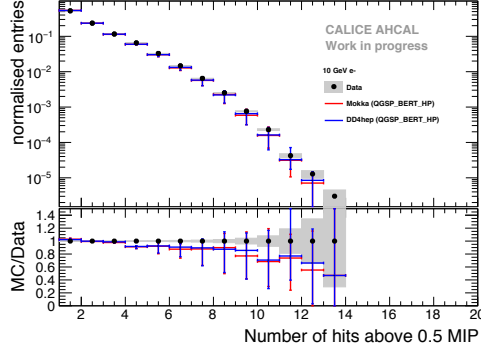
(a) 10 GeV.
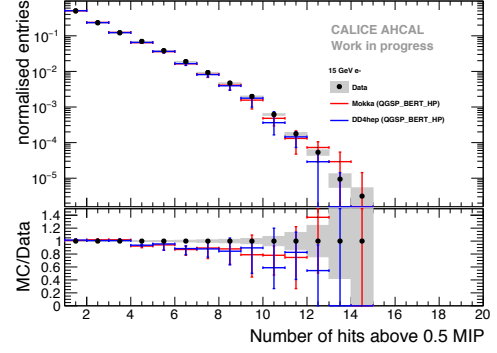
(b) 15 GeV.
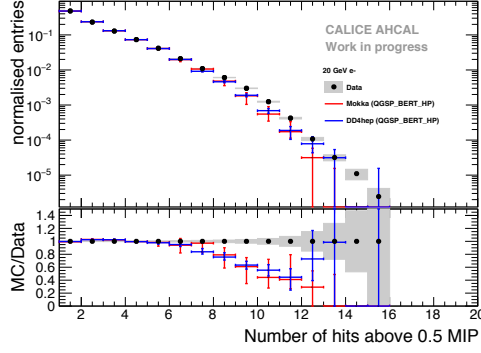
(c) 20 GeV.

(d) 30 GeV.

(e) 40 GeV.

(f) 50 GeV.

Figure 8.16 – Comparison between electron data and MC for all energies of the number of triggered channels per chip. The grey area represents the statistical error of the data. Error bars in simulation are obtained by varying the cross-talk parameter between 10% and 18%.

Chapter 9

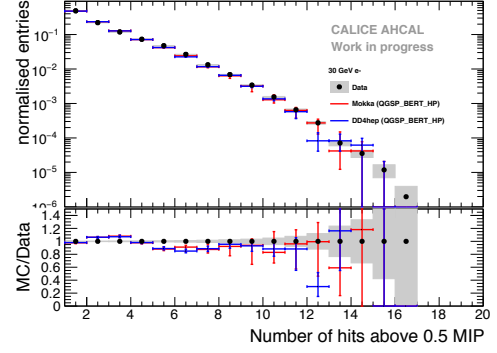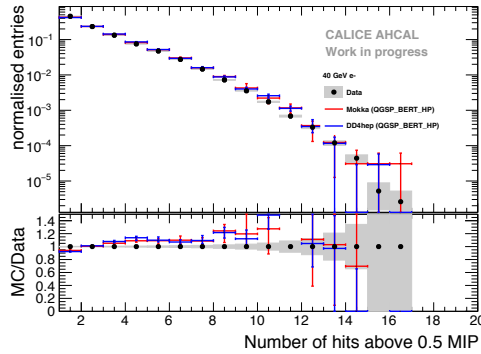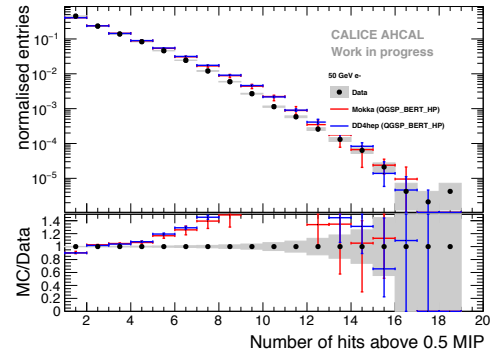# ILD detector simulation studies

Simulation of detector response is an essential part in high energy physics experiment. In Early stage of a project, simulations are done in order to explore and understand the possibilities of a detector design as well as its limitations. Simulation can be use as a way to determine requirements of an experiment to reach certain goals. During data-taking and afterwards, simulations are used model physics processes to compare the expected value from theory to a measured value for various processes.

In this chapter, software tools will be briefly introduced. The ILCSOFT framework used for this analysis will be described in **??**. The chain starts by the simulation of single kaons (K_L^0) interaction with the ILD detector model based on GEANT 4. Then simulated events undergoes the full chain reconstruction as explained in **??**. The procedure of the analysis (based on Marlin) and its conclusions will be presented in **??**. Finally, a benchmark of a fast simulation software (SGV) against the ILD full simulation will be described in **??**, particularly focussing on particle-flow performance aspects.

9.1 Simulation and software framework

9.1.1 ILCSOFT software framework

Various tools developed by the Linear Collider community is regrouped in a common software framework called ILCSOFT [15]. It provides a complete framework that can be used for Monte-Carlo studies and experiments. As an example, physics studies, ILD detector optimisation and performance for the ILC are performed under the ILCSOFT framework.

Table 9.1 – Considered ILD detector options.

Option	ECAL Technology	HCAL Technology
ILD_o1_v05	SiW-ECAL	AHCAL
ILD_o2_v05	SiW-ECAL	SDHCAL
ILD_o3_v05	Sc-ECAL	AHCAL

Most of the tools in the framework use an Event Data Model (EMD) named Linear Collider I/O (LCIO) which provides a reliable and performant solution for simulation and analysis studies [16]. With this tool, various detector concepts and analysis can be shared.

The ILCSOFT framework provides a modular C++ framework named MARLIN for reconstruction and analysis of physics events [17]. MARLIN uses LCIO seamlessly and is configured using XML steering files. MARLIN enables users to develop custom modules for their own and run it along other already existing modules.

The reconstruction and analysis tools used in this analysis are mostly part of ILCSOFT. For this thesis, ILCSOFT v01-17-11 was used for simulation, reconstruction and analysis.

9.1.2   ILD Detector Simulation

The following analysis is using one of the generic ILD detector model (ILD_o1_v05) as describe in **??** within the MOKKA framework. Many other models are also considered for ILD as shown in Table 9.1. MOKKA is a front-end to GEANT 4 and provides a realistic geometry of the ILD detector. The MOKKA version used is v08-05 and the GEANT 4 version is 10.01. The simulation is performed by simply using the particle gun provided in GEANT 4 to shoot particles (π^- or K_L^0) in different regions of the detector by randomly variating the angles θ and ϕ of the gun. To model hadronic showers, the QGSP_BERT physics list was used. The output of the simulation provides a lcio file containing collections of the tracking hits and simulated calorimeter hits. This file is then reconstructed within MARLIN.

9.2   Reconstruction chain

The reconstruction is done on simulated data in order to implement detector effects. For example, calorimeter hits need to be digitized by implementing threshold and readout effects.

9.2.1   Tracking

The tracking reconstruction is performed on each individual tracking detector. Track segments are identified by pattern recognition algorithms.

Track fitting is performed using the track segments with an inversed Kalman filter to identify trajectories of charged particles. Each tracks contains origin, direction, charge and momentum of the particle [18].

9.2.2   Calorimeter digitization

The calorimeter digitisation is performed on simulated calorimeter hits as part of ILD-CaloDigi processor [19]. It takes account for threshold effect from the electronics, sampling fraction of the calorimeter and the readout technology used. In the considered model of ILD, the SiW-ECAL and AHCAL are used.

In both cases, it uses a silicon-pixel based technology. The digitisation then takes into account the finite number of pixels that can be fired as well as the statistical fluctuations related to pixel readout [20].

Concerning time, it uses a simple digitisation. For a simulated hit, all contributions are looped over and only adds contributions under a certain timing cut (default is 100 ns). This modelisation of timing is very simplified as in reality the electronics are shaping the signal with a certain shapping time and register the time of the first contribution over the threshold (default is 0.5 MIP) **??**.

9.2.3   Pandora PFA

PandoraPFA [21] is the Particle Flow algorithm used for Linear Colliders as explained in **??**. It uses as input tracks and calorimeter hits to form Particle Flow Objects (PFO). It uses a complex multi-stage process but basically, calorimeter hits are clustered and associated to tracks (if any) then the energy of a cluster can be corrected to improve the energy resolution. If the right criterium are matched, it forms a PFO which contains information about the reconstructed objects.

9.3 Influence of time cuts on hadronic showers

In this section, a study of timing cuts on hadronic shower is performed. The goal of this study is to assess the influence of timing cuts on the properties of hadronics showers as for example the width of the shower as well as the needed time resolution. The study will be divided in 2 parts, the first part assuming a perfect time resolution and the second part assuming time resolution for different cases.

9.3.1 Modification of timing window in ILDCaloDigi

Timing of hits is registered in a very simplyfied way as explained in **??**. The modification of the time window (ranging from 1 ns to 100 ns) is performed during the reconstruction for different simulated K_L^0 energies (ranging from 5 to 90 GeV).

9.3.2 Effects of calibration constants and Pandora constants

Before studying the effect of timing on hadrons showers, a check was performed on the initial provided calibration constants of the ILD detector. Several constants are used for the digitisation and reconstruction (GeV to MIP, sampling, Pandora EM/Had constants...) in order to get the correct reconstructed energy. The plots below are selecting events with only one PFO and a $\cos \theta$ cut on the reconstructed particle of 0.7.

The figures 9.1a and 9.1b show the linearity and resolution curves for different sets of calibration constants at the cluster hit level i.e. looking at all the hits in a PFO cluster. Thus this enables to understand the effects of the digitisation constants in ILDDigiCalo though small clustering effects are present.

One can see that the blue and black curves are very similar due to the fact that no constants were changed in theses sets. Moreover the linearity is not perfect and varies between -15% and 5% also the curve crosses the line $x = y$ which if corrected would degrade the energy resolution. The green and red lines are similar as they have the same constants (the non-linearity correction is only applied to PFOs). The linearity fluctuates between -15% and -5% but does not cross the line $x = y$.

Concerning the energy resolution all the curves are very similar and are as expected. The green and red curves are slightly better due to the improvement of the calibration constants.
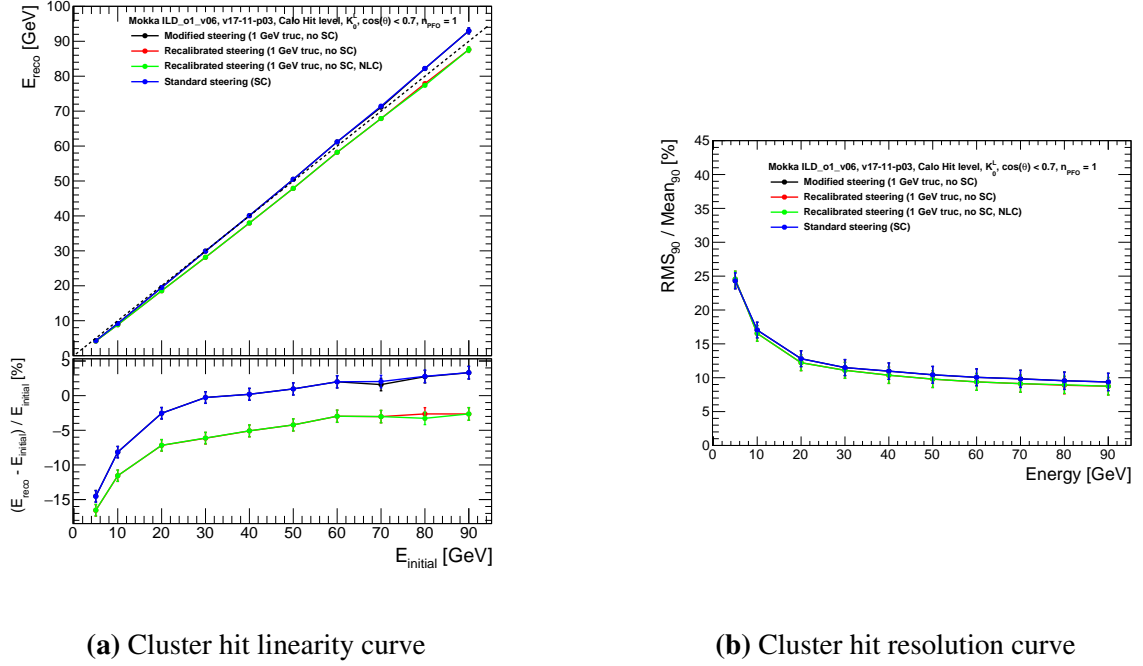
(a) Cluster hit linearity curve

(b) Cluster hit resolution curve

Figure 9.1 – a) The top plot shows the mean reconstructed energy E_{reco} for 5 to 90 GeV K^0_L function of the simulated energy $E_{initial}$ for different constant parameters used in the reconstruction at the cluster hit level. The bottom plot shows the relative difference of the different curves to the line $x = y$. b) The plot shows the relative resolution $RMS_{90}/Mean_{90}$ for different constant parameters used in the reconstruction function of the energy. The blue curve uses the standard calibration, the black curve uses a modified set of parameters using energy truncation and no SC, the red curve uses constant parameters after recalibration and the green curve uses the same parameters as the red curve with non-linearity correction. The error bars represent statistical uncertainties.

Another option is to look at the PFO level as shown in figures 9.2a and 9.2b. This permits to understand the effects of the calibration constants in PandoraPFA.

The plots show a different picture. For the linearity curve, the red and black line are quite similar and show a non-lineariy especially at high energies between -10% and 2%. The green line is nicely linear thanks to the non-linearity correction. Then the blue line is off by around 10%, this is believed to be due to the weights of the software conpensation that are not optimal for this model.

For the resolution curves, one can see a rise of the resolution at high energies for the red, green and black lines certainly due to the non-linearity. The blue curve present a bump after 50 GeV changing suddenly the slope of the curve due to the over-correction of the energy.

Through the linearity is not perfect over all energies, the most regarded observable is the
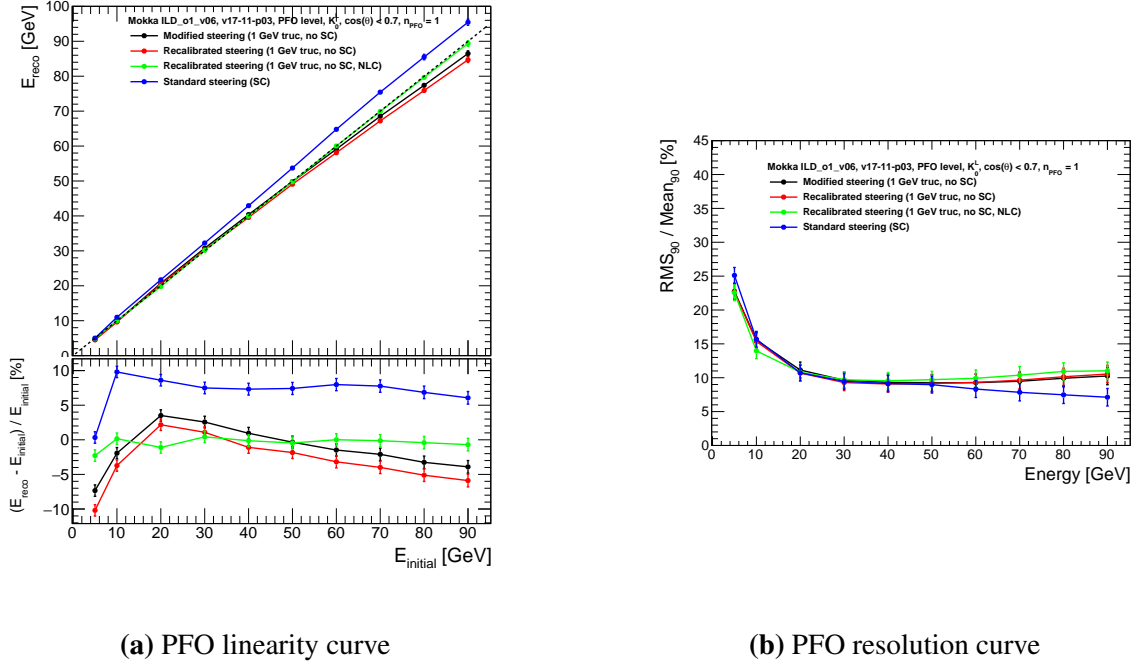
(a) PFO linearity curve

(b) PFO resolution curve

Figure 9.2 – a) The top plot shows the mean reconstructed energy E_{reco} for 5 to 90 GeV K_L^0 function of the simulated energy $E_{initial}$ for different constant parameters used in the reconstruction at the PFO level. The bottom plot shows the relative difference of the different curves to the line $x = y$. b) The plot shows the relative resolution $RMS_{90}/Mean_{90}$ for different constant parameters used in the reconstruction function of the energy. The blue curve uses the standard calibration, the black curve uses a modified set of parameters using energy truncation and no SC, the red curve uses constant parameters after recalibration and the green curve uses the same parameters as the red curve with non-linearity correction. The error bars represent statistical uncertainties.

jet energy resolution. As explained in **??**, jets are mostly composed of charged particles of around 60%. In this case, the energy of the PFO is coming from the track. Moreover neutral particles are counting in general for around 30% of the contribution in a jet.

As shown in figure 9.3a, for jets representative of heavy boson decay near production threshold, the momentum spectrum is dominant at around 10 GeV as for heavy boosted jets with a more complex event topology, the momentum distribution is still dominant to low energies but present a tail to much higher energies. Thus the non-linearity has only little effect there. It is still relevant to understand the different effects of the reconstruction at single particle level.

A complementary study was to look at the minimal distance between a charged and neutral particle for theses different physics processes. The figure 9.3b shows that for low energy jets the mean minimal distance (measured at the front face of the SiW-ECAL) be-
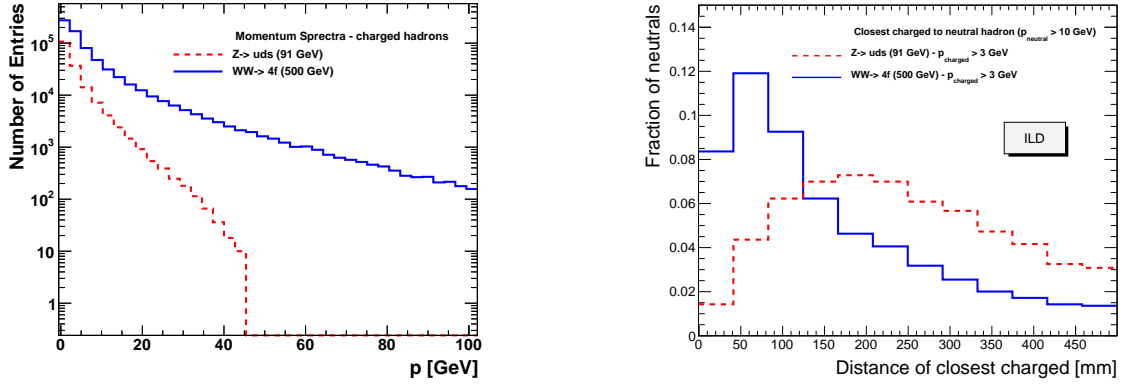
(a) Momentum spectrum of charged hadrons.

**(b)** Minimal distance between a charged and neutral particle at the front face of the ECAL.

Figure 9.3 – a) Momentum distribution for charged particles in simulated $e^+e^- \to Z/\gamma \to q\bar{q}$ with $q = u,d,s$ at $\sqrt{s} = 91$ GeV and $e^+e^- \to W^+W^- \to q\bar{q}q\bar{q}$ where q is a quark at $\sqrt{s} = 500$ GeV . b) Distribution of distances to the closest charged track for neutral particles produced in $Z/\gamma \to q\bar{q}$ and $W^+W^- \to q\bar{q}q\bar{q}$ processes measured at the front face of the electromagnetic calorimeter in the ILD detector.

tween a charged and neutral hadron is around 180 mm thus in this context, showers are well separated. But at higher energies where density is higher, typical distances of 50 mm need to be resolved. This situation can become relevant in the contribution of confusion to the jet energy resolution. In this case, the use of timing information could help to separate nearby showers and improve the pattern recognition.

9.3.3 Timing cut effects on hadronic showers in ILD detector

In this section, the effect of timing cuts on hadronic showers is investigated. The study was performed using the ILCSOFT framework for reconstruction and a personal MARLIN processor for analysis. In order to study the effect of timing on hadronic shower properties, the initial study was performed assuming a perfect timing resolution (i.e. the timing information is the Monte-Carlo truth). In a following step, several timing resolution were used to assess different scenarios. The smearing of the time was done by randomly sampling a normalised gaussian centered in 0 ns with a timing resolution denoted $\sigma_t = 0.4$, 1 and 8 ns.

The selection of events is fairly simple, only events in the barrel region ($cos\theta < 0.7$) are selected. All the calorimeter hits in the ECAL and HCAL are used.
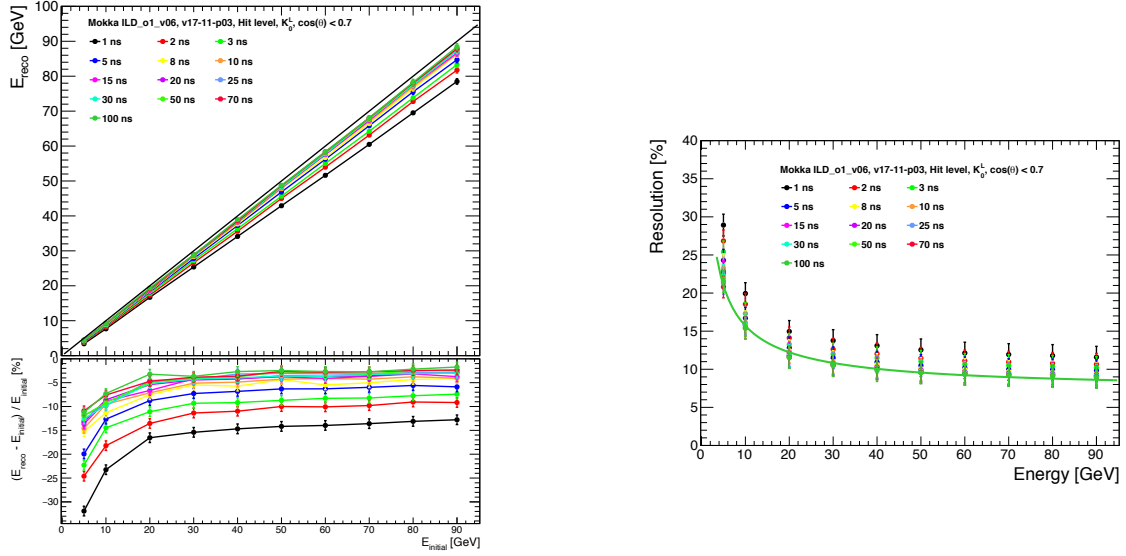
(a) Linearity curve with no time smearing.

(b) Resolution curve with no time smearing.

Figure 9.4 – a) The top plot represent the linearity curve in the ILD detector over a range of energy from 5 GeV to 90 GeV for different timing cuts assuming a perfect resolution. The bottom plot represent the relative deviation to the line $x = y$ for the different time cuts. b) The plot illustrates the relative energy resolution ($\frac{\sigma_E}{E}$) at single particle level for different timing cuts. The green line is a fit performed at $100\,\text{ns}$ of the form $\frac{\sigma_E}{E} = \frac{a}{\sqrt{E}} \bigoplus b$ where a is the stochastic term ($44.01\% \pm 3.17$) and b the constant term (7.26 ± 0.84).

9.3.3.1   On Monte-Carlo level

The following section present results of timing cuts assuming a perfect time resolution. To avoid any effects of clustering and Pandora, the study was performed at the calorimeter hit level. Several shower observables were looked at as a function of the time cut for energies from 5 GeV to 90 GeV K_L^0. The different time cuts used are: 1, 2, 3, 5, 8, 10, 15, 20, 25, 30, 50, 70 and $100\,\text{ns}$.

The figures 9.4a and 9.4b show the effect of timing cut on linearity and energy resolution. The tighter the timing cut gets, the linearity slope decreases and resolution gets degraded. This effectively means that with a harder timing cut, more hits of the shower are removed but mostly only outer hits carrying only a small fraction of the total shower energy, the core of the shower mostly does not get affected by timing cut up to few nanoseconds.

The figure 9.5 shows the relative impact on the energy resolution compared to the $100\,\text{ns}$ cut as function of timing cuts for all energies. The energy resolution is mostly not affected over a cut of around $20\,\text{ns}$ meaning that the removed hits are not carrying a lot of energy
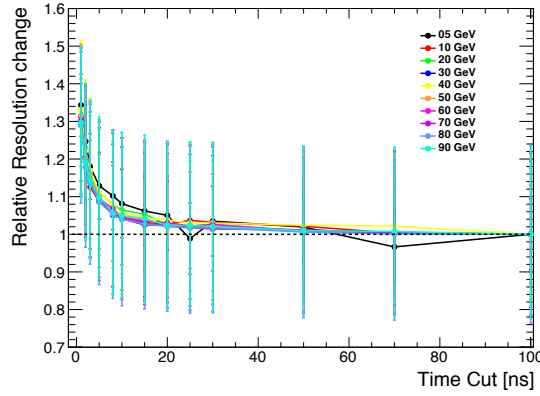
Figure 9.5 – Relative change of the energy resolution compared to 100 ns as function of the timing cut. The error bars represent the statistical uncertainty.

and are part of the shower halo. Then below 20 ns, the resolution starts to degrade slowly relatively in the same way for all energies. A hard cut of 1 ns will degrade greatly the energy resolution up to around 30%.

The figure **??** shows the radial profile of a 50 GeV hadronic shower. The radial profile of the shower is filled for each hit with the distance to the main shower axis (R_i, eq.9.1) weighted by the hit energy (E_i).

$$R_i = \sqrt{\Sigma_i (r_i - r_{cog})^2 - \|(\mathbf{r_i} - \mathbf{r_{cog}}) \cdot \mathbf{Eigen}\|^2)}$$
$$\text{with} \quad \mathbf{r_i} = (x_i, y_i, z_i) \quad \text{and} \quad \mathbf{r_{CoG}} = (cog_x, cog_y, cog_z)$$

(9.1)

The main part of the energy density is situated in the core within few centimeters. The influence of timing cuts is highly visible in the tail of the distribution (or halo of the shower) and as very little influence on the energy density deposited in core of the shower. Though an effect of increase of energy density in the two first bins of the distribution is visible. This effect is related to a displacement of the center of gravity (CoG) as function of the timing cut as outer hits of the shower are removed. This has been checked by looking at the hit radius distribution relative to a fixed reference instead of the CoG (the Monte-Carlo particle endpoint) as shown in figure 9.6b. One can observe that in this case, the timing cut removes only part of the tail and does not affect the core of the distribution.

Another aspect looked at was the influence of timing cut on the shower width <R>
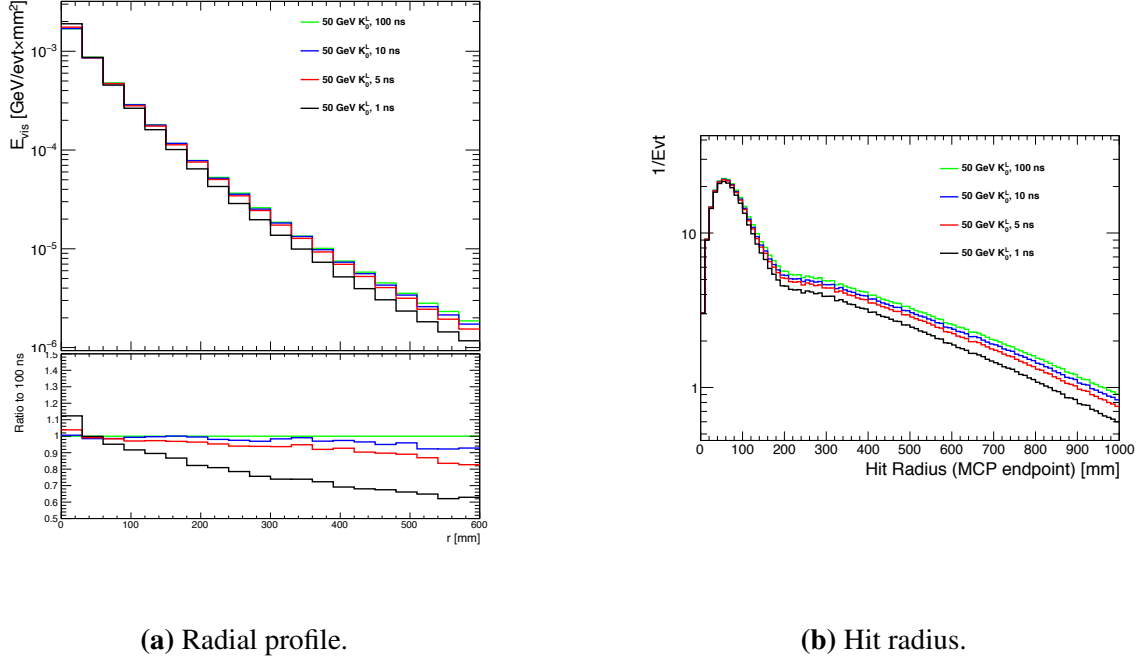
(a) Radial profile.

(b) Hit radius.

Figure 9.6 – a) The top plot shows the radial profile of a 50 GeV hadronic shower overlayed for different timing cuts. The bottom plot shows the ratio of the histograms to 100 ns radial profile. b) Hit radius histograms at 50 GeV for different timing cuts.

(eq.9.2) defined as:

$$<R>= \frac{\Sigma_i E_i r_i}{\Sigma_i E_i} \tag{9.2}$$

The figures 9.7a and 9.7b show the shower width <R> for different particle energies as function of the timing cut. It shows that a tight timing cut at 1 ns can reduce the shower width up to around 70%. One can observe also that the shower width at 5 and 10 GeV are behaving differently than higher than 10 GeV . This may come from the transition from the Bertini model (BERT) to the quark string gluon model (QGSP) in the physics list in this energy range. Looking at the shower width in absolute value, hadronic showers are wider at lower energies ($\sim$180 mm for 5 GeV) certainly due to the magnetic field. Applying a timing cut removes more and more hits from the halo of the shower, thus reducing its size up to a point where it reaches the core of the shower at $\sim$20 ns timing cut where the shower is around a couple of tiles in size. At this point, the shower width behaves similarly for all energies by reducing gradually the size of the core.

It is interresting to look at the gain in the reduction of the shower width compared to
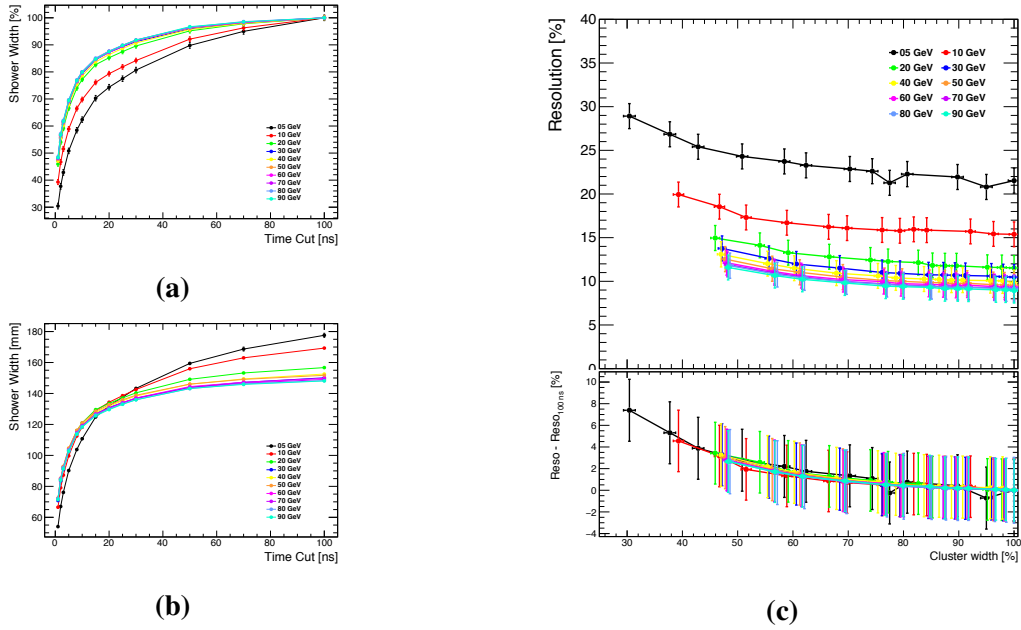
Figure 9.7 – a) The plot represents the mean of the shower width <R> as function of timing cut for different particle energies. The y-axis has been normalized to the shower width at 100 ns. The shower width decreases steadily as function of the timing cut, indicating that the shower gets narrower. b) The plots represents the absolute value of the mean shower width <R> in mm as function of the timing cut. This shows that the low energy showers are generally wider certainly due to the magnetic field. And under 20 ns, the width is very similar indicating the core of the shower is fairly similar for all energies. c) The top plot is the energy resolution as function of shower width for different particle energies. Each point represents a timing cut from 1 ns ns to 100 ns from left to right. The bottom plot is the loss of resolution compared to the gain in shower width size.

the loss in energy resolution. In fact, reducing the shower width would improve the pattern recognition in Pandora. The figure 9.7c shows the resolution loss as function of the shower width. The bottom plots shows the gain in shower width is behaving in the same way for all energies. The tigher the timing cut gets, the small the shower gets as well as a loss in resolution. The main point here is that the gain in shower width is great (up to 60-70%) compared to the loss in energy resolution (up to 8%) that could be recovered in a next step after pattern recognition.

This study shows that the use of timing cuts give a great advantage in order to improve pattern recognition without degrading too much the energy resolution of a hadronic shower. However, this study assumes a perfect timing resolution which doesń reflect the reality. In the next section, different time resolution were assumed based on the current knowledge on the timing resolution of the foreseen electronics.

Table 9.2 – Time resolution used for smearing.

Scenario	Time resolution (ns)
Testbeam	8
Ideal	1
ILC extrapolated	0.4

9.3.3.2   In a realistic scenario

In this section, a similar study is performed as in section **??**. Instead it assumes realistic time resolutions based on the current electronic technology. The table 9.2 sums up the investigated time resolutions. The same selection is applied as in the previous section.

The testbeam resolution is the time resolution obtained with the current AHCAL technological prototype as explained in section **??**. The ideal time resolution is in the order of the time scale of the development of hadronic showers. And finally, the ILC extrapolated is obtained by assuming a linear extrapolation from the tesbeam time resolution with a faster slow clock of 5 MHz instead of 250 kHz (x20 faster) as explained in **??**.

Looking at the impact on linearity and energy resolution, time resolution in the order of sub-nanosecond does not affect much the linearity and resolution as shown in figures 9.8a and 9.9a. For a time resolution in the nanosecond order, the figures 9.8b and 9.9b show that a tight timing cut of 1-2 ns will start to affect linearity and resolution. However, for timing resolution higher, the linearity and resolution, as shown in figures 9.8c and 9.9c, start to get heavily degraded for timing cuts below 10-20 ns. This tells that at least a time resolution of around 1 ns is needed in order to use time information without impacting calorimeter performance too much.

Looking back again at the resolution as function of the shower width, one can notice that in the case of (sub-)nanosecond scale time resolution, the loss of resolution is minimal compared to the shower width. A timing cut of around 1-2 ns would only degrade the energy resolution of around 8-10% but would decrease the shower width by 60% as shown in figures 9.10a and 9.10b. On the other side, a time resolution of 8 ns would yield only a reduction of 40% of the shower width for the same loss in resolution corresponding to a timing cut of 10 ns as shown in figure 9.10c.

9.3.3.3 Conclusion

The study presented in this section demonstrates that timing information can be used in hadronic showers in order to improve pattern recognition and at last the jet energy resolution by reducing the confusion term. This study was performed assuming different time resolutions and shows that in order to benefit from timing information, a time resolution for the electronics in the (sub-)nanosecond scale would be ideal. Assuming a time resolution of 1 ns, a time cut around 1-2 ns would greatly reduce the shower width by about 60% and would degrade the energy resolution by about 8% as well as the linearity by decreasing the slope which could be corrected.

Higher time resolution would certainly help but would impact too a certain level the calorimeter energy resolution. One would need to think how to implement the use of time information in Pandora in order to improve the pattern recongnition efficiently.
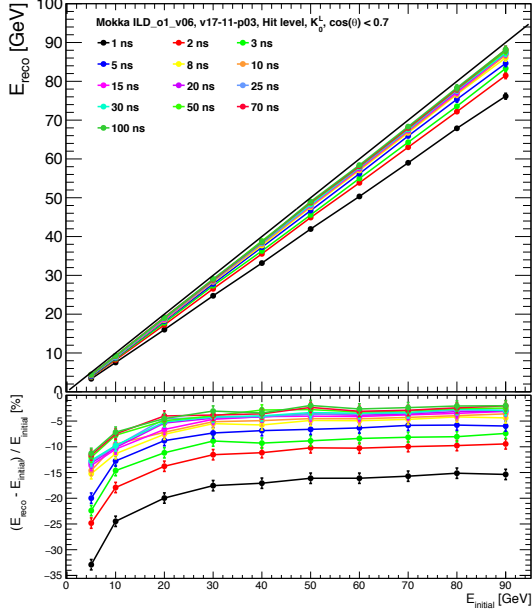
(a) 0.4 ns time smearing.
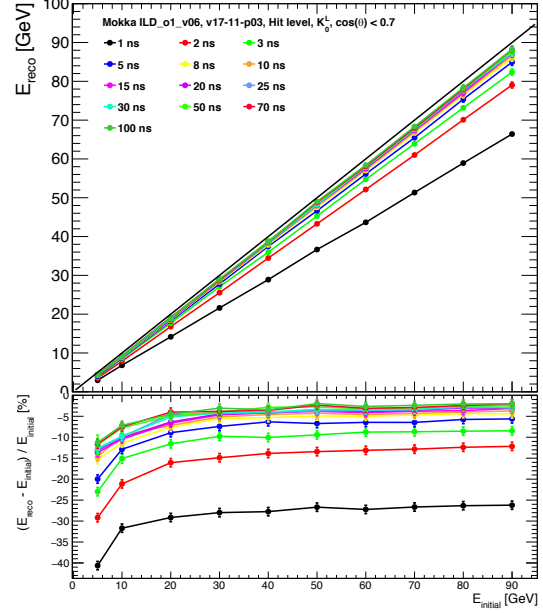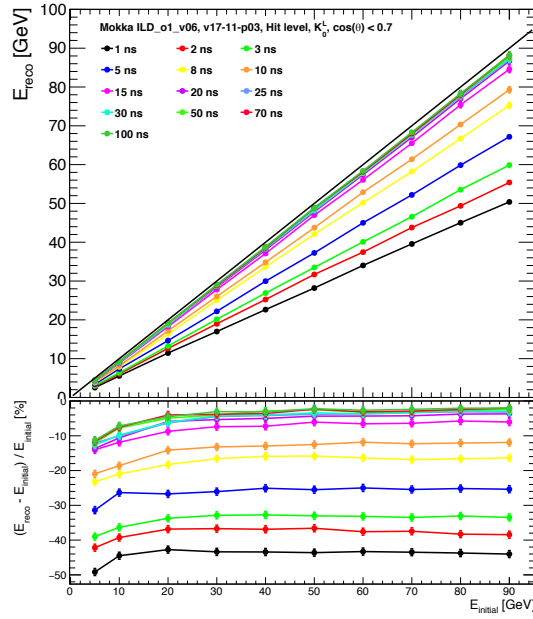
(b) 1 ns time smearing.

(c) 8 ns time smearing.

Figure 9.8 – Linearity curves for different assumed time resolutions (0.4 to 8 ns from left to right). The top plot represents the mean reconstructed energy E_{reco} for kaons from 5 to 90 GeV . The bottom plot shows the relative deviation to the line $x = y$.

(a) 0.4 ns time smearing.

(b) 1 ns time smearing.

(c) 8 ns time smearing.

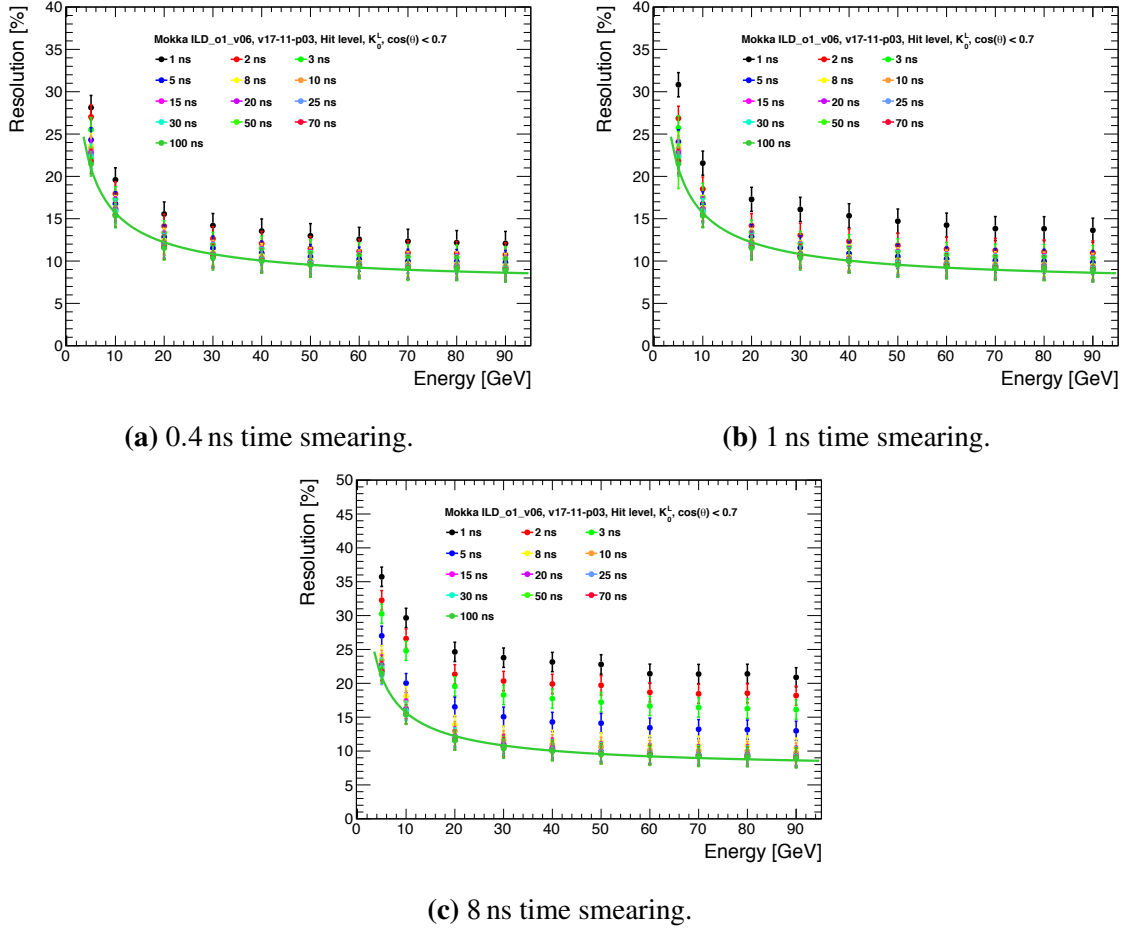**Figure 9.9** – Energy resolution curves for different assumed time resolutions (0.4 to 8 ns from left to right). The plot represents the relative energy resolution $\frac{\sigma_E}{E}$ for kaons from 5 to 90 GeV for each timing cut. The green line is a fit applied to 100 ns timing cut of the typical form $\frac{\sigma_E}{E} = \frac{a}{\sqrt{E}} \bigoplus b$.
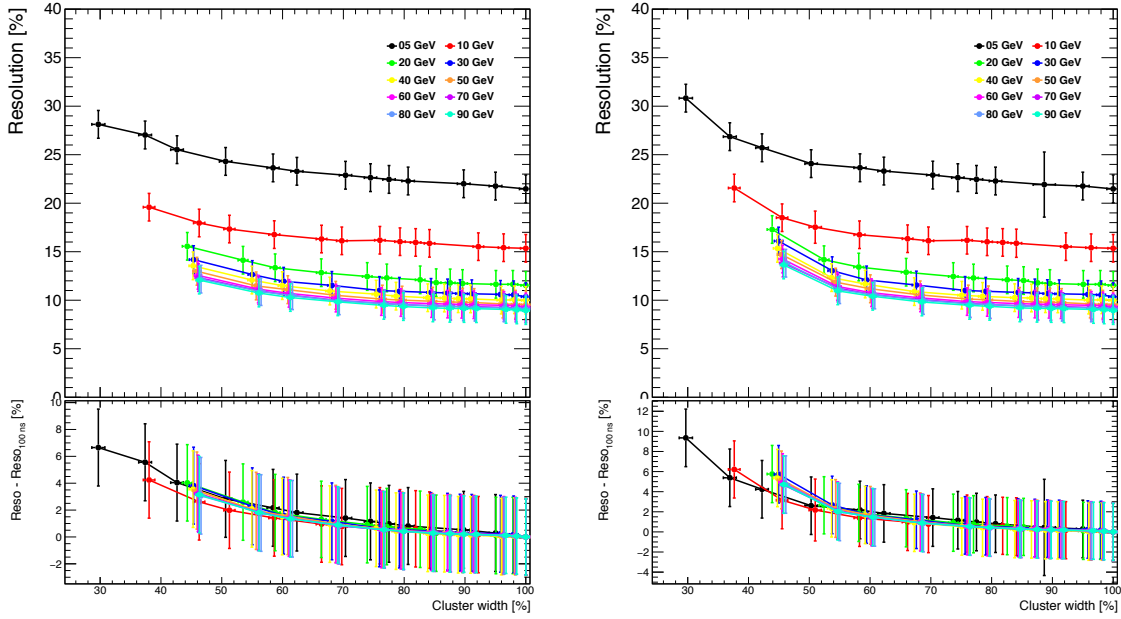
(a) 0.4 ns time smearing.
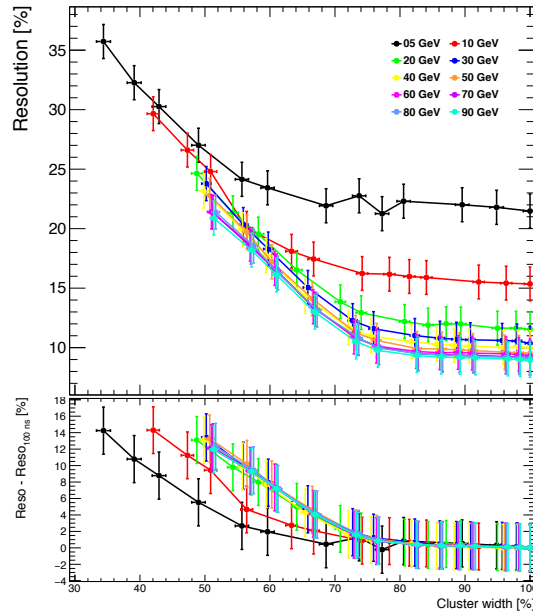
(b) 1 ns time smearing.

(c) 8 ns time smearing.

Figure 9.10 – Energy resolution as function of the shower width for different assumed time resolutions (0.4 to 8 ns from left to right). The top plot shows the relative energy resolution $\frac{\sigma_E}{E}$ for kaons from 5 to 90 GeV where each point is representing a timing cut as function of the shower width. The bottom plot shows the deviation to the nominal resolution at 100 ns as a function of the shower width.

Chapter 10

Particle Flow studies in full and fast simulation

Particle Flow is a new approach to calorimetry in order to achieve a jet energy resolution much better than traditional calorimetry approaches (order of twice better). It has a potential to revolutionise particle detector design for future lepton collider experiment. Particle Flow has the ability of reconstructing the energy of all the individual contributions inside a jet as described in section **??**.

In simulation, Particle Flow has been implemented known as Pandora PFA in the full ILD simulation. One further approach is the use of fast simulation. Why using fast simulation? In simple words, it is much faster i.e. a ttbar event takes few seconds compared to minutes in full simulation. Like that several studies could be done with much faster speed and variation of observables like in SUSY scenarios much easier while keeping a precision close to the full simulation.

Currently, several fast detector simulations exist. SGV (Simulation a Grande Vitesse) is one of them which is developed by Mikael Berggren [22]. It is a fast detector simulation program using covariance matrix calculations. The status of SGV is that it performs already very well compared to full simulation and also integrates a Particle Flow Parametrisation in order to simulate Pandora PFA.

In this section, I will focus on the performance of SGV compared to full simulation and the Particle Flow parametrisation performance in SGV. This will enable to spot where SGV matchs up to the full simulation as well where it fails and improving the current particle flow parametrisation.
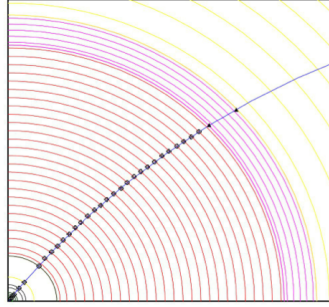
Figure 10.1 – Tracking in SGV [22]. The tracker is represented by pseudo-layers at which intersection with a track, the covariance matrix is calculated, going from the outer part of the tracker to the inner part (inversed Kalman filter).

10.1   Particle Flow in SGV

Fast detector simulation can use different types or methods in order to simulate particle interactions with the detector. For any of them, the response can be simulated in the same time order as to generate an event (i.e. around 10 ms).

For this, a four momentum smearing method can be done assuming global detector properties. More elaborate, a parametric simulation (like SIMDET [23]) can be used, where the response depends on the energy of the particle and its angle. And finally, covariance matrix calculations can be performed using the detector layout and the generated particles. SGV is found in this category.

10.1.1   Tracking in SGV

In general, a track is calculated by the intersection of the helix of a particle with pseudo-layers describing the material in the tracker. From the outermost hit, an helix is parametrised and then propagated to the next inner layer and the intersection and covariance matrix are calculated, the propagation is done until the inner most layer is reached.

In SGV, there is no definition of hits. The helix is followed through the detector to find which pseudo-layers are hit by the particle as shown in figure 10.1. The tracking is done until the intersection of the start of the innermost calorimeter is reached. At each intersected pseudo-layers, the covariance matrix of the track is calculated. The covariance matrix is then translated along the particle trajectory and multiple scattering effects are included into the calculation.

In basic, it is what a Kalman filter [24] is doing but not in the formal way. The track fitted is matched to the vertex and the perigee parameters are then smeared according to the

calculated covariance matrix. The tracking efficiency is parametrised from the full simulation.

10.1.2 Calorimeter Simulation

For the calorimeter simulation, the particle is extrapolated to the intersections with the calorimeters. At this point, a decision is made:

- It is detected as a Minimum Ionising Particle (MIP).

- It initiates an electromagnetic shower or a hadronic shower.

- It is below the detector threshold.

According to the decision, the detector response is simulated from different parameters i.e. energy, type of particle, detector region... Some parameters are controlled by steering files. Calorimeter showers can be merged if they are close to each others. To go towards more realism, the simulation of confusion between clusters can be done (Particle Flow parametrisation).

10.1.3 SGV Particle Flow parametrisation

In SGV, usual errors are already implemented i.e on detected energy, shower position and shape. However, there are association errors. Clusters might be merged, split or get associated to the wrong track.

If (a part of) a neutral cluster is wrongly associated to a charged track (so then considered as a charged cluster), energy is then lost as shown in figure 10.2a. On the other hand, if (a part of) a charged cluster is not associated to any track (considered then as a neutral cluster), the energy is double counted as shown in figure 10.2b. Theses mis-associations give rise to an error on the total energy of an event and the particle momentum [25].

The study of these association errors was done by using the Letter of Intent (LOI) mass produced samples from full simulation using the particle flow algorithm PandoraPFA [26]. The most relevant observables were identified as: the cluster energy, the distance of the nearest particle of the other type(i.e. neutral-to-charged or charged-to-neutral), whether the particle was a hadron or not, and whether it would be detected in the barrel or endcap calorimeters. The confusion was factorized in 4 sub-processes [22]:

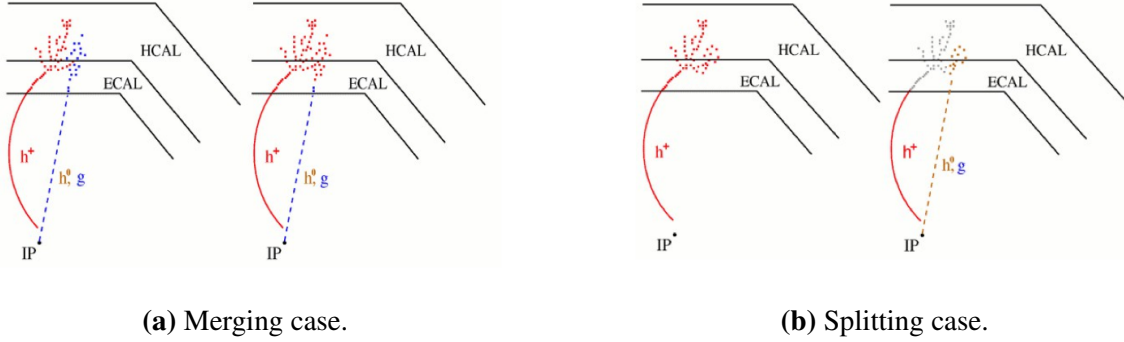- The probability of a cluster to split or merge as seen in figure 10.3.

(a) Merging case.

(b) Splitting case.

Figure 10.2 – a) If the cluster is merged, energy is lost. b) If the cluster is split, energy is double-counted.

- In case of splitting, a probability to split off/merge the **entire** cluster.

- In case of splitting but not completely, a function of the fraction of split off.

From this, probability distribution functions are derived (figures 10.4a and 10.4b). The algorithm is applied in the Particle Flow parametrisation of SGV. So far, the results seems to be in a good agreement mostly for the neutrals but still some development is needed to get the best agreement possible between SGV and the full simulation.

10.2 Benchmarking of fast simulation

10.2.1 Event Preparation

The following study was perform on a simulated data sample from the Detailed Baseline Report (DBD) of $e^+e^- \to W^+W^- \to q\bar{q}q\bar{q}$ at 500 GeV center of mass energy as shown on figure 10.5. It is particularly interesting in order to evaluate the separation between the two W bosons and the full hadronic decay complicating the reconstruction. This sample includes a $\gamma\gamma \to hadrons$ background overlay. Several preparatory steps are performed during the reconstruction. First, a procedure is done to remove the overlay. Then hits are clustered into jets.

10.2.1.1 Jet finding

In the final state of the process $e^+e^- \to W^+W^- \to q\bar{q}q\bar{q}$, there are four primary quarks. These quarks will fragment and hadronise to form hadronic jets. Moreover, background
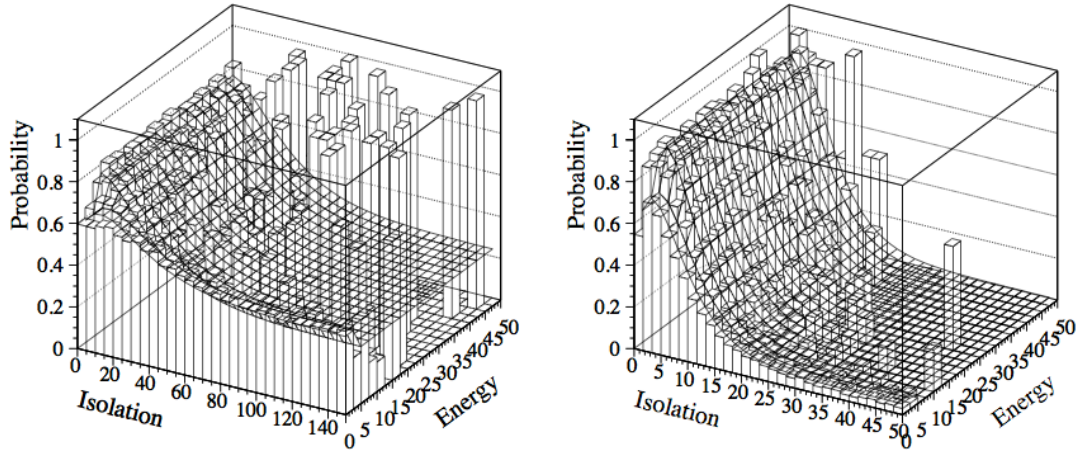
Figure 10.3 – Probability distribution of splitting in function of the cluster energy and the type of the particle.

such as $\gamma\gamma \rightarrow$ *hadrons* may deteriorate the jet energy resolution. Thus, jet finding is very important in the event preparation.

A jet finding package called SATORUJETFINDER was used as part of the MARLINRECO package available in ILCSOFT. The jet finder uses an algorithm called Durham [27, 28]. This algorithm is based on JADE algorithm. It utilizes a binary joining scheme by computing the distance d_{ij} between two clusters i and j as:

$$d_{ij} = 2min(E_i, E_j)(1 - cos\theta_{ij}) \tag{10.1}$$

where $E_{i,j}$ is the energy of cluster i, j and θ_{ij} is the opening angle between the momentum vectors of the clusters i, j. If d_{ij} is below d_{cut}, the clusters are combined such as $p_k = p_i + p_j$ with $p_{i,j,k} = (E_{i,j,k}, \mathbf{p_{i,j,k}})$, commonly called the $E - scheme$. This procedure is repeated until all pair of clusters are above d_{cut}. The final pair is called a jet.

For this analysis, the number of jets required is 4 due to the topology of the event. Each jets are stored as a RECONSTRUCTED OBJECT in LCIO. These objects include the four momenta of the jets $(E, \mathbf{p})$ as well as each individual particle properties in a jet can be accessed.
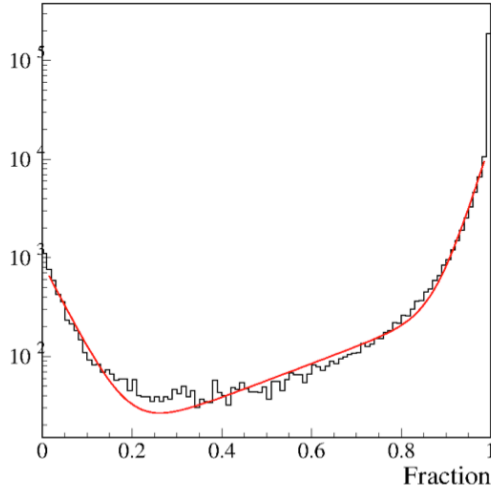
(a) Fitting of the probability of merging for photons.
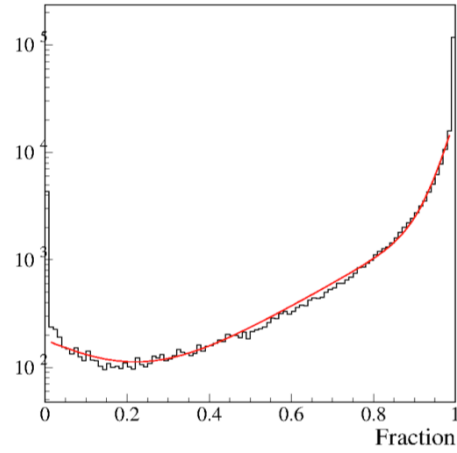
(b) Fitting of the probability of splitting for charged hadrons.

Figure 10.4 – a) . b) .

10.2.1.2 $\gamma\gamma$ overlay removal

For this analysis, no $\gamma\gamma$ overlay removal method was used as Monte-Carlo information can be accessed and used during the analysis as described in the next subsection **??**.

But commonly, a k_T-algorithm can be used to remove it before the jet finding procedure. The hadrons created in the interaction of photon beams are very close to the initial beams and have almost no transverse energy. Therefore, this background looks like ̈jetsälong the beam line. A k_T-algorithm in *exclusive* mode is used to detect and remove these particles. The algorithm takes the jet radius R parameter (in the order of 1) and the total number of expected jets as input. The number of expected jets and two additional for the jets along the beam line is shown to work best [29].

10.2.1.3 LCIOᴛᴏRᴏᴏᴛ package

In order to perform the analysis, a final package called LCIOᴛᴏRᴏᴏᴛ provided by Mickael Bergreen was used. This package is categorising the LCIO Objects (PFO, Jets, Clusters...) into ROOT user-specific classes i.e. *xRoot-TrueParticles* for Monte-Carlo level particle information. Moreover, this package includes a link between Clusters, PFO, Tracks and MC particles to know for example to which MC and/or PFO particle a track belongs to.
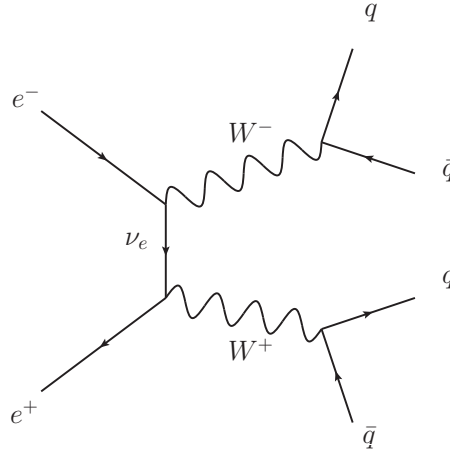
Figure 10.5 – Tree level Feymann diagram for the process $e^+e^- \to W^+W^- \to q\bar{q}q\bar{q}$ at $\sqrt{s}$ = 500 GeV .

10.2.2 Tracking efficiency

Before reconstructing particles, PandoraPFA applies a selection on the tracks that can be a candidate for a Particle Flow Object (PFO). In this selection, PandoraPFA assumes that everything is a pion as a first guess, which is mostly true in most cases.

Particles coming from V0s as the decay of a neutral particle in flight i.e. $\gamma \to e^+e^-$, kinks as the decay of a particle into another particle of the same charge with lower momentum giving a change in the curvature i.e. $\pi^+ \to \mu^+ + \nu$ or Prongs as the decay of a τ are identified in a first place and treated separately. Pandora PFA uses a track selection code in order to categorise them into multi parameters categories :

- CanFormPFO

- CanFormClusterlessPFO

- CannotFormPFO

To perform the categorisation, PandoraPFA applies several cuts on the track. First, it checks the number of hits of the track in the tracking chamber (TPC) and the forward tracker. The number of hits in the TPC must be between 5 and 5000 hits, in the forward tracker, a number of expected hits is calculated based on the geometry of the forward tracker if the angle of the track ($\tan\lambda$) is within the acceptance of the forward tracker.

Then, the algorithm checks if the track reaches the front face of the electromagnetic calorimeter. The conditions are that the radius of the outermost hit or the max z position of

all hits is above a minimum radius defined by the SET layer (R_{min}^{SET}) or minimum z defined by the ETD layer (Z_{min}^{ETD}). Or if there is a sufficient number of hits in the TPC (11) or FTD (4). If the track has a low transverse momentum, meaning that the track may curl inside the inner tracker, that the cosine angle of the track is within the acceptance of the TPC. Or that the transverse momentum of the track is above the threshold $0.3 \times B \times \frac{R_{outer}^{TPC}}{2000}$.

If the track survive all these cuts, a quality check is performed on the tracks parameters: curvature (Ω), impact parameter (d_0), z position at the point of closest approach or p.c.a (z_0), radius of innermost hit (r_{min}) and the track energy (E_{track}). The curvature must be different from 0, the momentum uncertainty $\frac{\sigma_p}{p}$ must be under 15%. If the track momentum p is over 1 GeV , the transverse momentum p_T and the momentum projected on the z axis p_Z must be different of 0 GeV and finally the number of TPC or FTD hits must be over a certain value. For TPC hits, an expected number of hits is calculated based on the geometry and the track momentum and compared to the number of measured TPC hits. For FTD hits, the number must be more than 2 hits.

Once a track passes the quality checks, Pandora categorise the track on cut-based differentiation. If a track has $d_0 < 50$ mm, $z_0 < 50$ mm and $r_{min} < R_{inner}^{TPC} + 50$ mm, the track is then categorised as ***CanFormPFO***.

A second criterion is used for non-vertex tracks i.e. tracks that are not matching the primary vertex, a check on $z_{min} - z_0$ where z_{min} is the z position of the first tracker hit and the r_{min} of the track is done. If the track passes through the cuts, it is flagged also as ***CanFormPFO***. If a track with unmatched vertex track has $d_0 < 5$ mm, $z_0 < 5$ mm, $r_{min} < R_{inner}^{TPC}$ + 50 mm and the track energy E_{track} is less than 5 GeV , the track is then categorised as ***CanFormClusterlessPFO***. For obvious reasons, tracks matching these criteria can end up in the category ***CanFormPFO***. This is then disentangled later by the track-cluster matching. For tracks that are categorised as V0s, kinks or prongs, they are also flagged as ***CanFormPFO*** or ***CanFormClusterlessPFO*** depending on the same criteria above. All the others tracks that do not meet the criteria are then flagged ***CannotFormPFO***, theses tracks will then not form any PFO in the reconstruction.

The goal was to check if whether Pandora rejects tracks with a PFO in SGV. As in SGV, no information is provided on the state of the track at a specific point or no tracker hit information is stored, only the relevant part of the selection made by PandoraPFA was applied. After the pseudo-selection, histograms ($h_{selected}$) for each track parameter (d_0, z_0, $cos\theta$ and p_T) were filled. For tracks that have the flag ïnPFOm̈eaning that the track was indeed used by Pandora and formed a PFO, histograms (h_{inPFO}) with the track parameters were also filled.
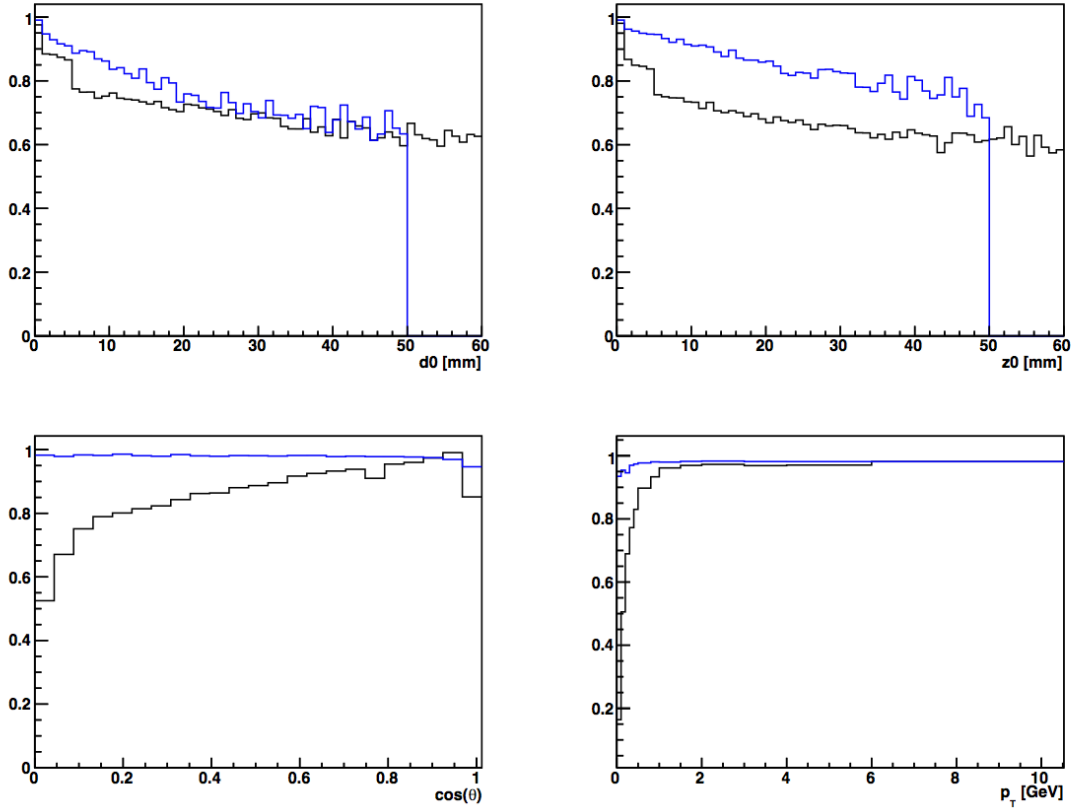
Figure 10.6 – Ratio ε for the track parameters d_0, z_0, $cos\theta$ and p_T. The full simulation is represented by a black line. SGV fast simulation is represented by a blue line.

To compared the performance of SGV to full simulation, a ratio ε was defined as $\varepsilon = \frac{h_{inPFO}}{h_{selected}}$ for the full simulation. In SGV, all tracks are by default forming a PFO. With the pseudo-selection, a certain number of tracks may be rejected thus with the ratio definition above, it may be over 1. In that case, for SGV, the ratio was defined as $\varepsilon = \frac{h_{selected}}{h_{inPFO}}$. The ratios for each track parameter are shown in figure 10.6.

As expected for the full simulation, the impact parameter (d_0) and the z position at the p.c.a (z_0) ratio plots are more or less constant. As for SGV, it seems to drop steeper but still matches quite well the full simulation. For the transverse mommentum p_T, SGV has a better ratio but this is more or less dependant on the geometry parametrisation of SGV which is relevant for low transverse momentum particles.

The main difference appears for the $cos\theta$ parameter, the full simulation seems to drop very much for very low angles compared to SGV. After further investigation, theses tracks are curlers in the TPC that make through until the endcap. At this reconstruction step, theses tracks are considered by Pandora to be able to form a PFO but further a matching between
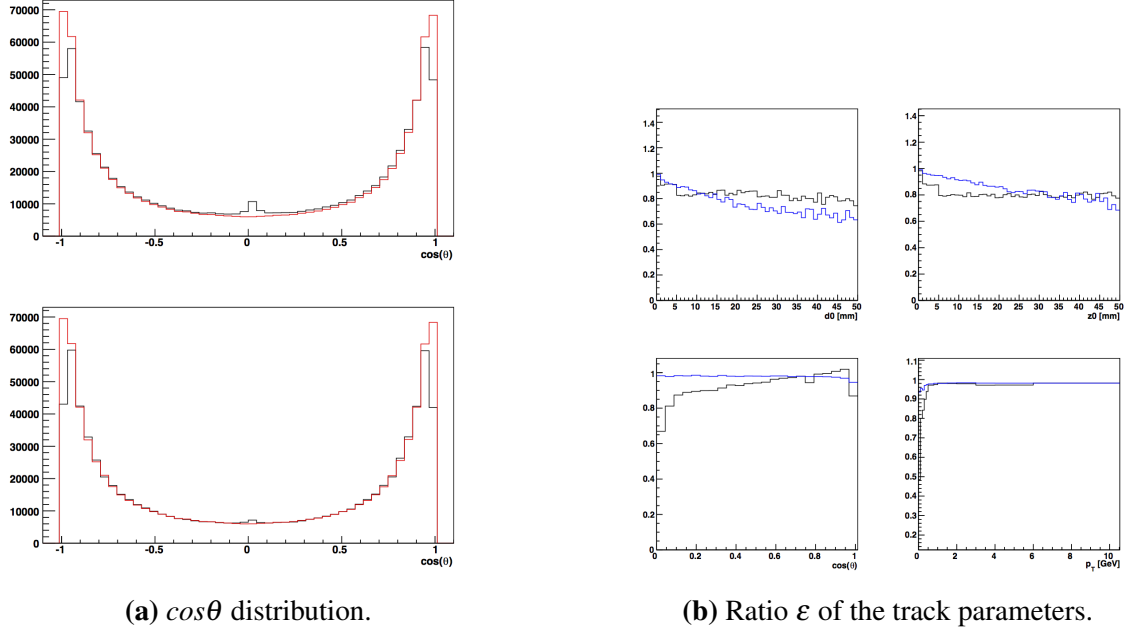
(a) $cos\theta$ distribution.

(b) Ratio ε of the track parameters.

Figure 10.7 – a) The top plot shows the $cos\theta$ distribution of MC tracks in red and Pandora track in blue with the pseudo-selection in SGV. The bottom plot shows the $cos\theta$ distribution of MC tracks in red and Pandora track in blue with the pseudo-selection and an additional cut on z_{min} to remove curling tracks in SGV. b) Ratio ε of the track parameters d_0, z_0, $cos\theta$ and p_T after additional cut on curling tracks. The black line represent the full simulation and the blue line represent SGV fast simulation.

clusters and track enables to get rid of most of theses curling tracks. A cut on $z_{min} - z_0$ that should be less than half a turn of the helix can get rid of most of theses curlers as shown in figures 10.7a and 10.7b.

By adding this cut, SGV and the full simulation agrees better. Nevertheless, the introduced cut seems still not enough to get rid of most of the curlers looking at the $cos(\theta)$ distribution. This shows that the tracking selection in PandoraPFA is not responsible for the observed discrepancy.

10.2.3   Track multiplicity and Correlation track/energy

A look at the number of tracks or multiplicity inside a jet was performed in order to see if SGV performs as expected. The number of tracks were counted per jet energy bins for full simulation, SGV with and without the Particle Flow parametrisation as shown on figure 10.8.

One can see that the multiplicity of tracks are in very good agreement between SGV
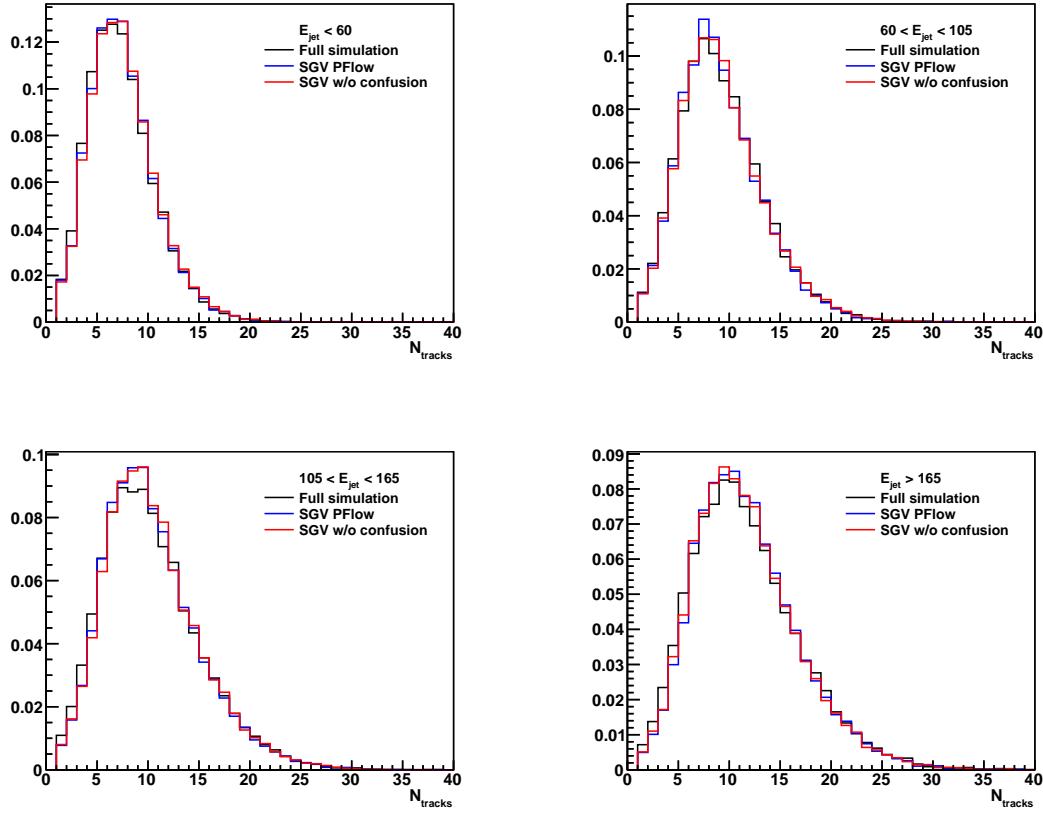
Figure 10.8 – Track Multiplicity in bins of jet energy. The full simulation is in black line, SGV without the particle flow parametrisation is in red and SGV with the parametrisation is in blue. The results in SGV are in a very good agreement with the full simulation.

and full simulation. Here the particle paramtrisation has a minimal impact on the pattern recognition and the association track-cluster as shown by the blue and red lines which are very similar.

Typically, jets are composed of 60-70% of charged particles, 10% of photons and 20-30% of neutrals. The correlation between the fraction of charged energy in a jet and track multiplicity was also looked at. The distributions shown on figures 10.9a and 10.9b are in agreement and correspond to what is expected.
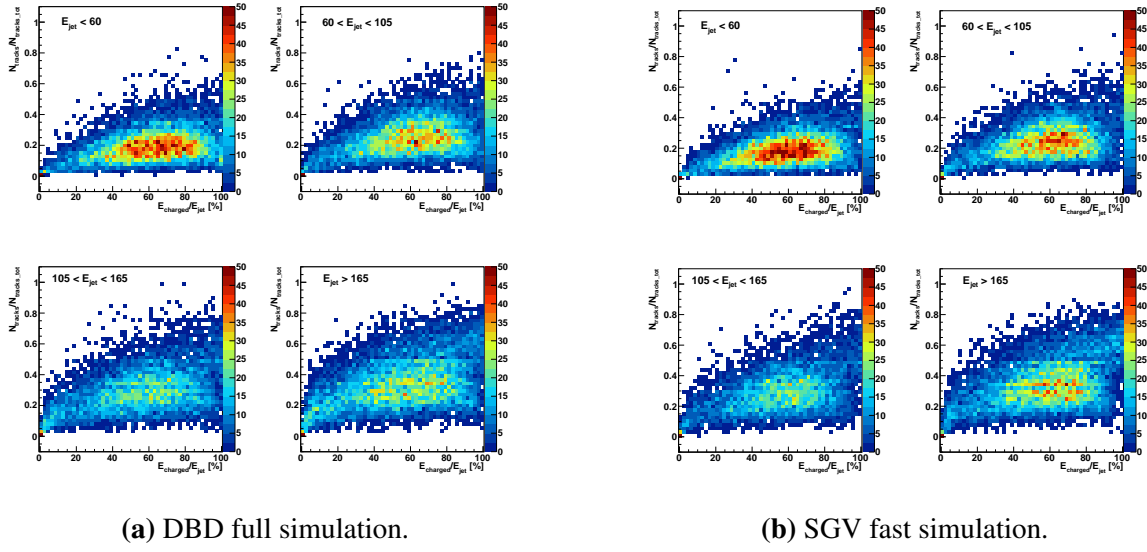
(a) DBD full simulation.

(b) SGV fast simulation.

Figure 10.9 – a) Correlation track multiplicity normalised to the total number of tracks versus the charged energy normalised to the jet energy for different jet energy bins for the full simulation. b) Correlation track multiplicity normalised to the total number of tracks versus the charged energy normalised to the jet energy for different jet energy bins for SGV.

10.3 Particle Flow studies

10.3.1 Double counted and lost energy

Association errors can happen during reconstruction as explained in section **??** because of a confusion term coming from the overlap of showers into the calorimeters.

The figure 10.10 revells 2 regions, the top right corner and the bottom left corner. The top right corner represents the region where there is almost no confusion between a track and the Monte-Carlo particle associated. There is almost a one-to-one relation between a track and a true particle, i.e., one true particle is associated to a track. The bottom left corner is the region where the confusion dominates, this region shows that it is difficult to associate correctly a particle to a track, the contributions to a track seem to come from different particles.

The goal of particle flow is to avoid confusion as much as possible. There can be different points of view concerning the treatment of the double counted and lost energy:

- At a cluster-track level by comparing the energy of a track (momentum + assumption of π mass) to the energy of the cluster associated to the track (it would be then an energy flow point of view).
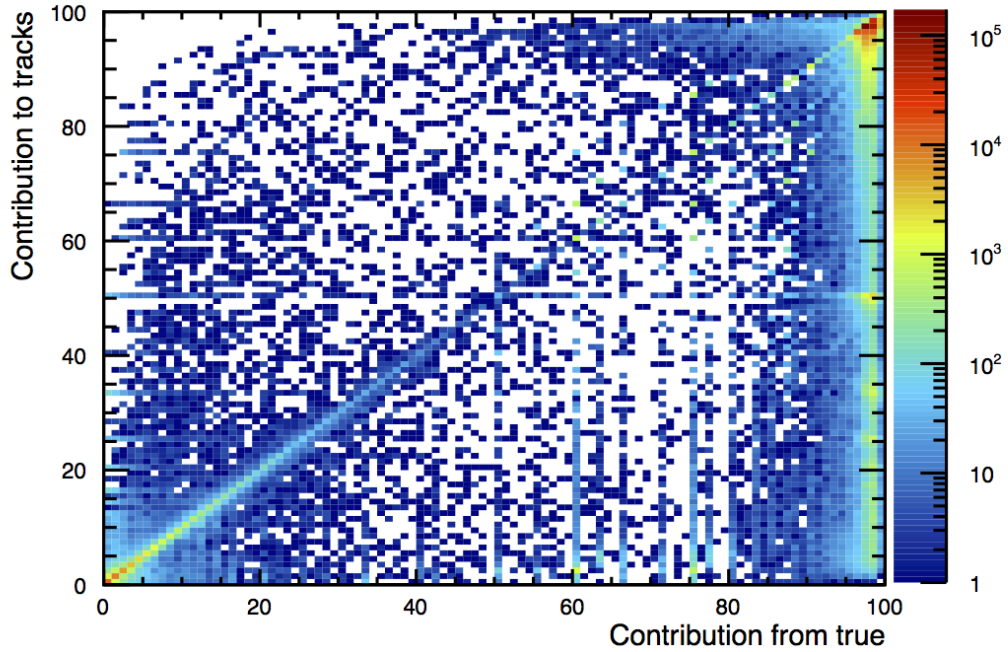
Figure 10.10 – Distribution of the weights of track-true particle relation. The contribution from true represent the contribution of a true particle to a track in terms of hits from this true particle compared to the total hits in the track and the contribution to track represent the inverse relation, the number of hits from a true particle compared to the total of simulated hits from this true particle.

- At a jet level (clusters contained into a jet) by looking at the double counted and lost energy over the jet energy.

10.3.1.1 At Cluster-Track level

At a Cluster-Track level, the following method has been pursued. For each event, each reconstructed particle is taken, then one look at the track associated to the reconstructed particle and calculate the track energy as:

$$E_{track} = \sqrt{\|\overrightarrow{p}\| \cdot \|\overrightarrow{p}\| + m_\pi^2} \qquad (10.2)$$

with $m_\pi = 0.139$ GeV and $\overrightarrow{p}$, the reconstructed particle momentum. The pion assumption is made like in PandoraPFA which in most cases is not wrong and will not affect the calculated energy by much. Then the cluster associated to the reconstructed particle is looked at and

the energy of the cluster $E_{cluster}$ is taken. A comparison between the track energy E_{track} and the cluster energy $E_{cluster}$ then is done.

If $E_{track} < E_{cluster}$, the difference is categorized as double-counted energy. Naturally the energy of the cluster should be the track energy because the resolution of the tracker is much better than the calorimeter. So if there is more energy in the cluster it means that a part of it may come from a near neutral particle or from a mis-measurement. If the opposite is true i.e. $E_{track} > E_{cluster}$, then it is categorized as lost energy. The double counted and lost energy is summed up for all the particles in the event. This method is done for each reconstructed particles in an event, thus for each event we have a point E_{dc} and E_{lost}. The result is shown on figure 10.11.

In the full simulation, it seems that PandoraPFA is leveling between the lost and double counted energy. Pandora may balancing both quantities on event by event basis. For SGV, the correlation is very similar with the parametrisation. SGV is has a tendency to have more double counting energy than lost energy indicating that SGV tends to split more clusters.

Looking at the total energy as shown on figure 10.12, SGV without the particle flow parametrisation seems to describe well the total energy but doesn't include the reconstruction effects explaining the smaller width of the distribution. When the parametrisation is used, a tail in the total energy appears. Though the width of the distribution seems correct, a shift in energy is visible. Therefore, the energy distribution of neutral and charged reconstructed particles was looked at as shown on figure 10.13.

The neutral energy distribution improves in SGV with the particle flow parametrisation and agrees well with the full simulation. But for the charged energy, the parametrisation doesn't change anything. This is expected because only the track information matters in this case and not the cluster in the calorimeters. The distribution is shifted to higher energies explaining the tail observed in the total energy distribution. This gives a hint that the parametrisation should have an effect on the charged particles. Which can be possible in the case that the track information is rejected (i.e. due to a bad track fitting) and only the calorimeter information is taken into account. Therefore, the same quantities were looked at the jet energy level in order to see at what energy scale the discrepancy appears.

10.3.1.2   At Jet level

The process $e^+e^- \to W^+W^- \to q\bar{q}q\bar{q}$ at $\sqrt{s} = 500$ GeV has a typical topology of 4 jets from the 4 primary quarks. The jets are obtained by running the Durham algorithm after the reconstruction. The Durham algorithm is a k_T-algorithm, it clusters all reconstructed particles into jets as explained in section **??**.

First, jets are classified into few energy bins for each event: 0 to 60 GeV , 60 to 105 GeV , 105 to 165 GeV and over 165 GeV . The energy bins were selected in order to have the same order of number of events per jet energy bin as seen on figure 10.14. Then, inside each jet, each reconstructed particle is taken. The same method as the section above is used. Now, E_{lost} and E_{dc} were calculated per jet. At the end, the lost energy versus the double-counted energy are normalised to the jet energy as shown on figures 10.15a and 10.15b.

For low jet energies, SGV and the full simulation seems to be in agreement. On the other hand, the higher the jet energy is, the more differences become visible. For jet energies over 165 GeV , SGV is double-counting much more than the full simulation which stays with a good correlation between E_{dc} and E_{lost}. This gives an indication that SGV is failing in regions where jet energies are high, over 165 GeV .

The reason could be that, in these cases, the energy density in the calorimeter is so high. So that the association errors can be committed more easily because the confusion term of the overlapping showers is getting bigger and bigger in function of the jet energy. PandoraPFA, to solve this problem, may be switching to a pure Ënergy Flowmode. Meaning that it is discarding the track information and only keeps the calorimeter information. And by reclustering, PandoraPFA is matching the overall energy in a calorimeter region to the tracks in the same region.

This may indicate that the current parametrisation can be improved and that the merging and splitting probabilities should be then function of the energy density in the calorimeter region studied.

10.3.2   Energy fraction inside a jet

Jets are composed of many charged and neutral particles. For each jet energy bin, the distribution of the charged/neutral energy fraction to the jet energy was looked at. It could give a handle in order to understand the effect of the parametrisation on a jet level and the observed discrepencies between the full simulation and SGV.

For the energy distribution on figures 10.16a and 10.16b, one can observe that the plots of neutral and charged energy are mirror to each other, as the sum of the charged and neutral energy should be equal to the jet energy. For low energy jets, the distributions seems to be rather in a good agreement, only small discrepancies are visible in the low/high fraction regions. For higher jet energies, this discrepancy is getting bigger. There is more neutral energy in the 50-70% region and much less in the 10-20% region for charged particles. Somehow SGV is pulling the energy in the wrong direction by splitting too much charged

clusters.

The idea is that charged energy from the 50+% region should be transferred to the 10-20% region, meaning that charged clusters are transformed to neutral clusters. That is how the total charged energy distribution could be shifted toward lower energies by ïosingc̈harged energy and gaining neutral energy. This is consistent with the assumption that PandoraPFA is switching to an Ënergy flowm̈ode. It can occurs during this process that charged cluster are transformed to neutral cluster in order to match the E/p locally. PandoraPFA only takes care of the calorimeter information and discards the track information.

10.3.3 Occupancy and Energy density

One relative variable in the splitting and merging probabilities is the distance between a cluster of one type (hadronic or electromagnetic) and a cluster of the other type. The study of the distribution of the distance to the nearest neighbour was performed distinguishing between ECAL and HCAL, basically electromagnetic and hadronic showers.

The procedure is perform such as in each jet, a list of neutral and charged particles is filled. Each of theses particles are projected either on the barrel or the endcap of the ECAL or HCAL depending on the nature of the cluster (EM or hadronic). The projection is done in order to calculate distances on the same geometry planes as SGV and the full simulation have slight different geometries. For neutrals, a simple calculation is done assuming a propagation at the speed of light. The intersection is calculated at the ECAL/HCAL endcap front face ($z_{ECAL} = 2450mm$ / $z_{HCAL} = 2650mm$) or ECAL/HCAL barrel front face ($r_{ECAL} = 1843mm$ / $r_{HCAL} = 2058mm$) according to ILD geometry as described in section **??**. For charged, the LCIO track is propagated following the helix parametrisation until the front face of the ECAL/HCAL in the endcap or barrel.

After this, the list of neutrals is looped over and the distance to all charged particles:

$$r_{ij} = \sqrt{(x_i - x_j)^2 + (y_i - y_j)^2 + (z_i - z_j)^2} \tag{10.3}$$

with $x_{i,j}$, $y_{i,j}$, $z_{i,j}$ the coordinates of the neutral particle i and any charged particle j at the front face of the ECAL/HCAL is calculated. A distinction between endcap and barrel is done to get rid of corner effects. The minimum distance d_{min} is defined as $min(r_{ij})$ for each neutral particle. The plots are shown on figures 10.17a and 10.17b.

One can observe that there is a discrepancy between full simulation and SGV with Particle Flow in the ECAL. The Particle Flow parametrisation seems to have the effect that particles are placed closer in the ECAL. On the other hand, the Particle Flow parametrisa-

tion seems to have a rather good effect in the HCAL. Thus the PFA parametrisation was disable for the ECAL and the same distributions were looked again as shown on figures **??** and **??**.

In that case, the distributions are in rather good agreement for the ECAL and HCAL. The Particle Flow parametrisation seems to have a rather limited effect on the ECAL distribution compared to SGV without Particle Flow.

Is the parametrisation of Particle Flow in SGV useless for the ECAL? In order to check the influence of the parametrisation on the ECAL energy distribution, the charged and neutral energy were looked at again. As expected, switching off the Particle Flow parametrisation for the ECAL have rather no or limited impact on the charged energy distribution as shown on figure 10.18.

One variable to look at would be the occupancy of the detector in the jet region or the energy density. This is could give us a clue to understand how PandoraPFA is splitting and merging in function of the energy density and then implement or correct the splitting and merging probabilities used in SGV to parametrise Particle Flow.

In conclusion, the benchmark of the fast simulation SGV was done. A Particle Flow parametrisation is implemented in SGV and most of the results obtained are in agreement with the full simulation. Still the parametrisation is not perfectly correct as there is still some discrepancies between SGV and the full simulation (Total energy, distance to the nearest neighbour, correlation between E_{dc} and E_{lost}...).

The next steps would be to look at the energy density distribution in a jet region and parametrise the splitting and merging probabilities of a cluster in function of the density and achieve an even better agreement between SGV and the full simulation.
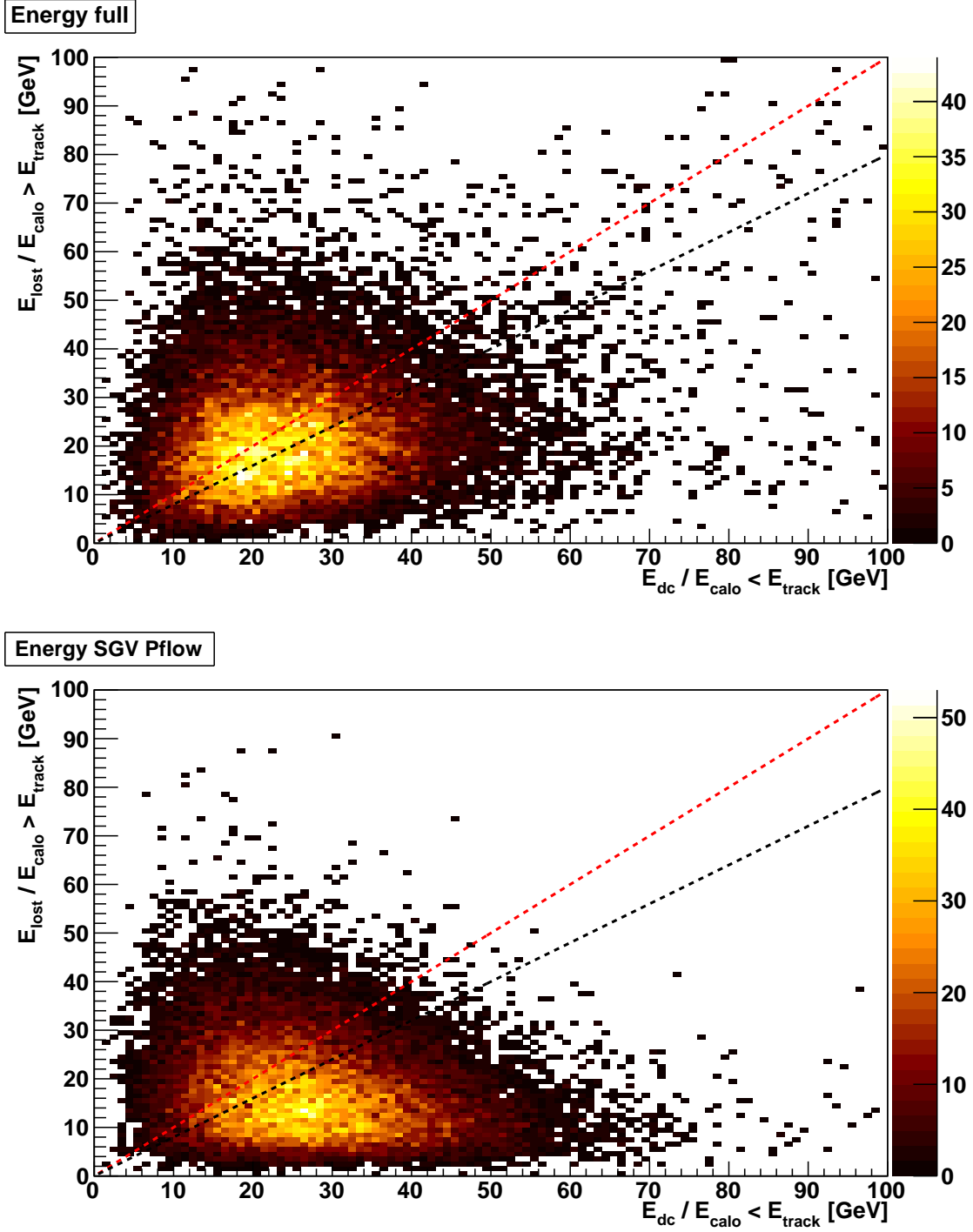
Figure 10.11 – 2D plot representing the lost energy versus the double-counted energy. The top plot is the full simulation and the bottom plot is SGV fast simulation. Each point in this plot represents an event. The red and the black dotted line indicate a correlation of 100% and 80%. One can observe that there is slightly different correlations for SGV and the full simulation.
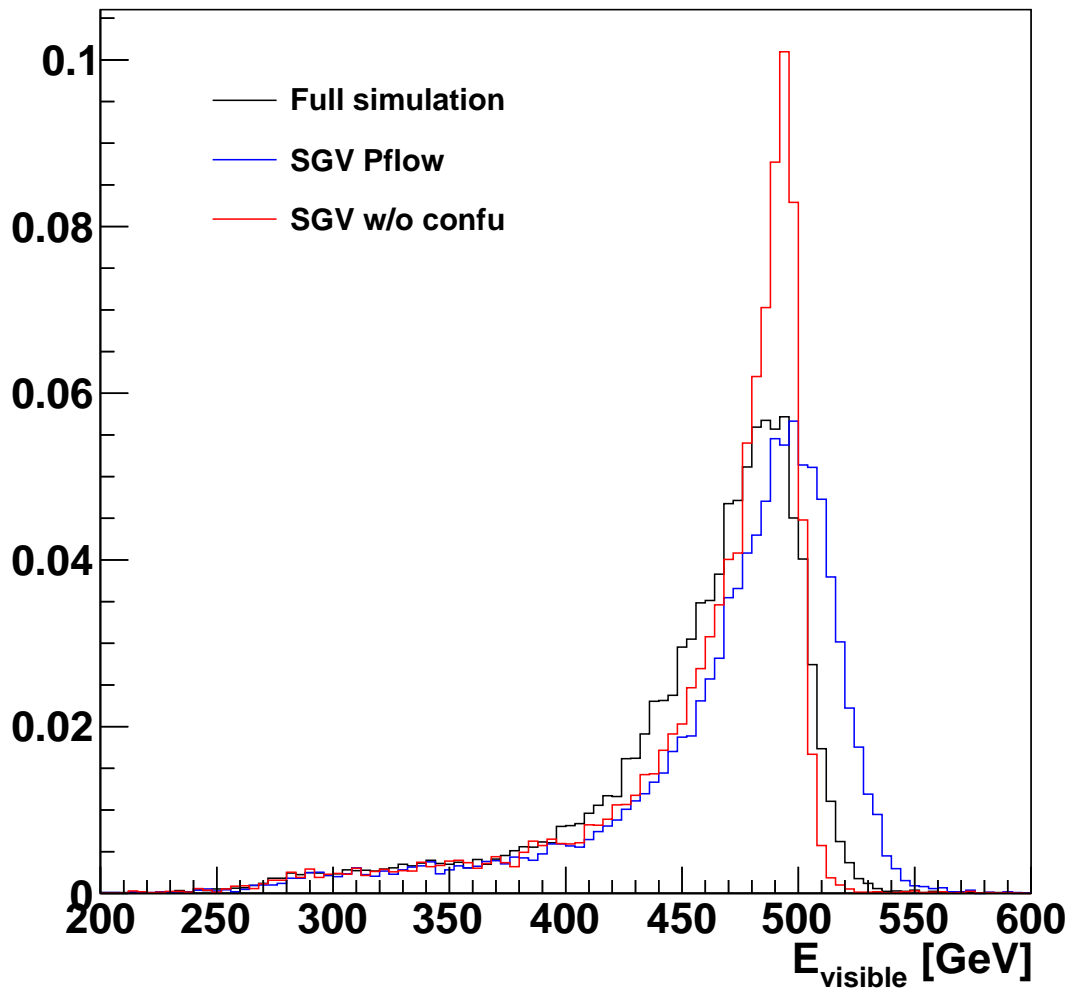
Visible Energy

Figure 10.12 – Representation of the total energy of all events for the full simulation in black line and SGV with (in blue line) and without the particle flow parametrisation (in red line).
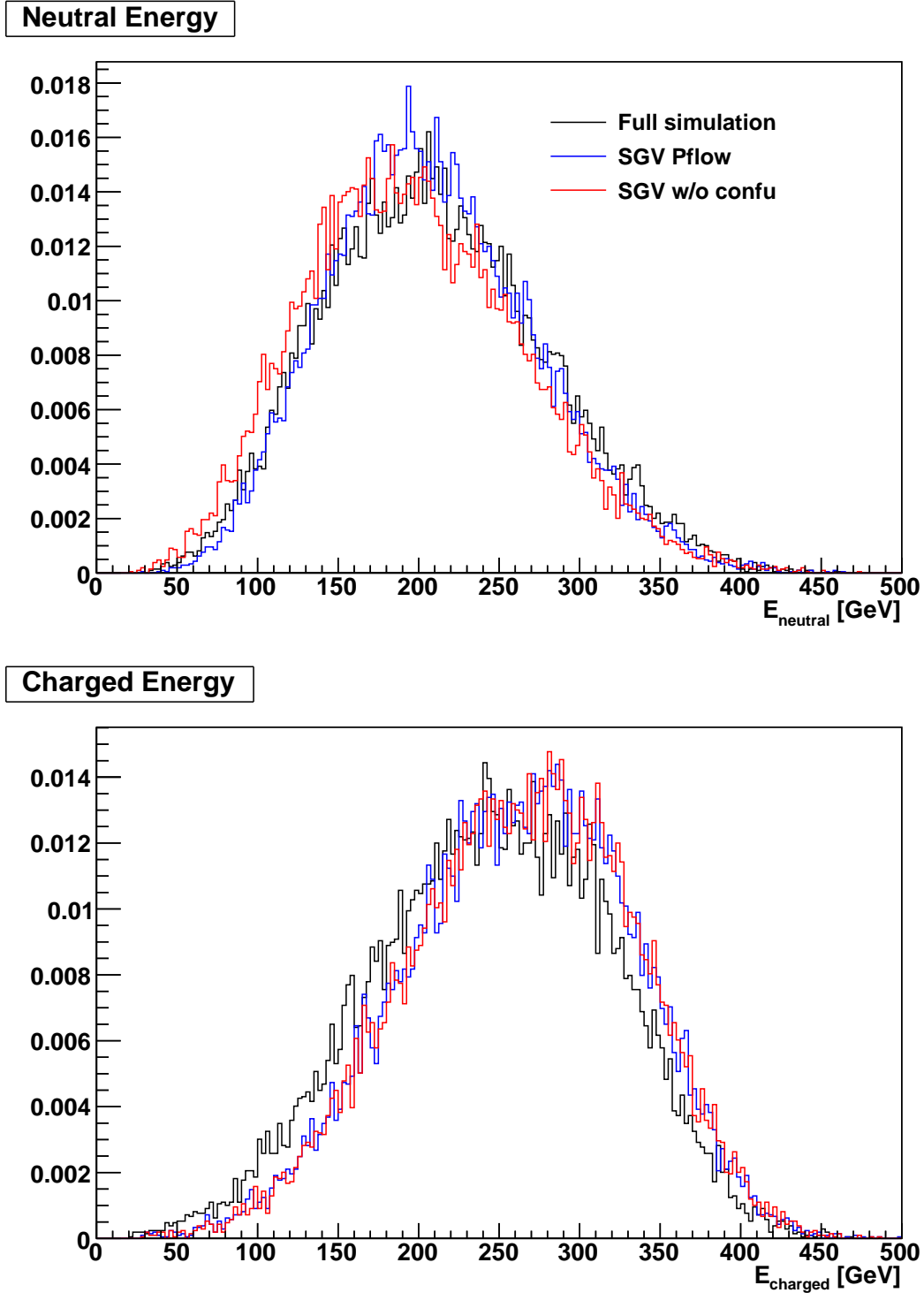
Neutral Energy

Charged Energy

Figure 10.13 – The top plot represents the total charged reconstructed particle energy. The bottom plot represents the total neutral reconstructed particle energy. SGV is indicated by a blue line (red line) with the particle flow parametrisation (without respectively) and the full simulation in black line.
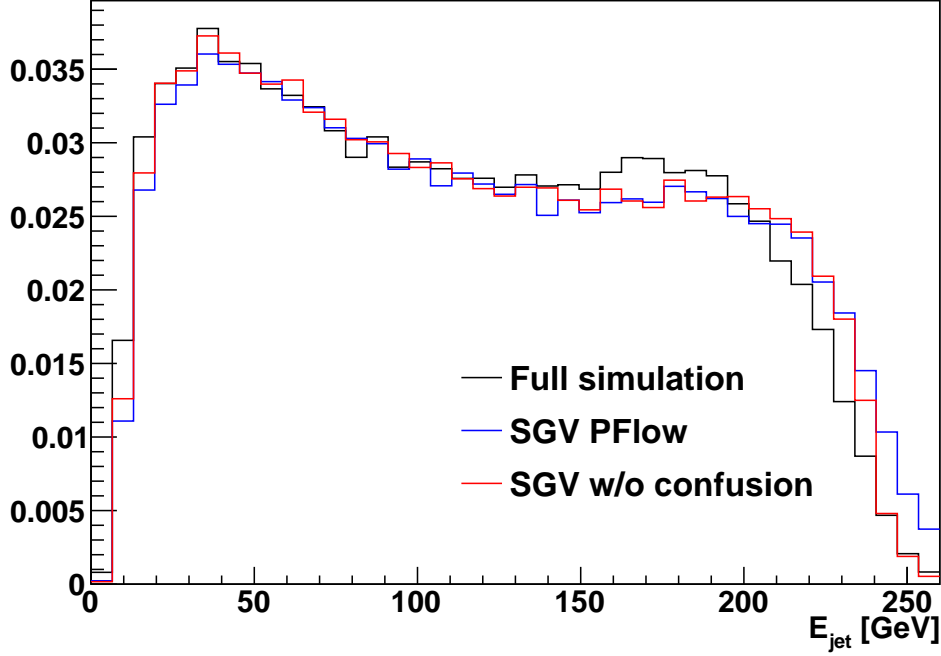
Figure 10.14 – Jet energy spectrum between the full simulation in black line and SGV in blue (red) line with (without) the particle flow parametrisation.
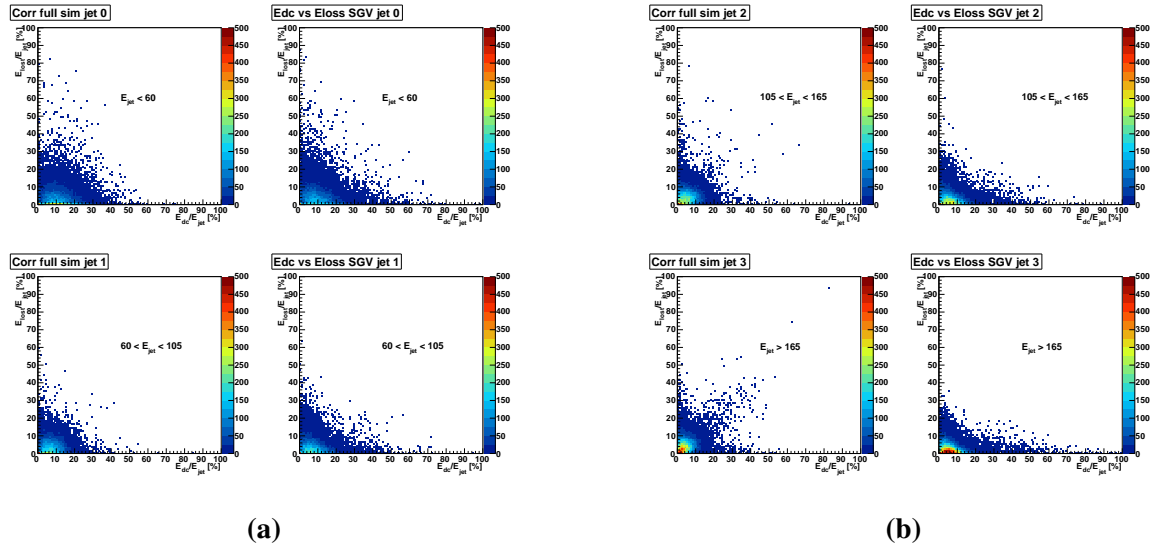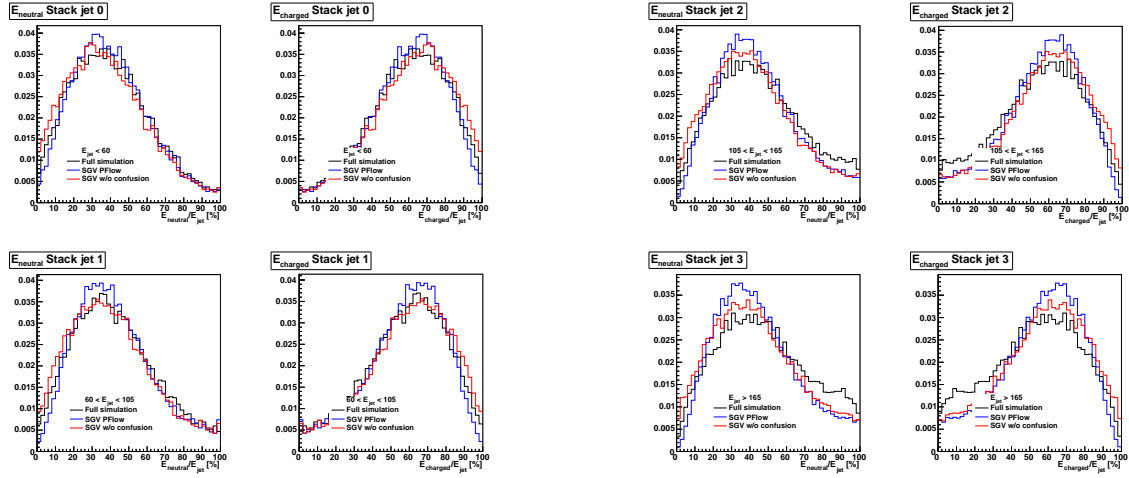

Figure 10.15 – a) Correlation between E_{lost} and E_{dc} for the full simulation. b) Correlation between E_{lost} and E_{dc} for SGV fast simulation.

(a) Energy distribution for charged and neutrals normalised to the jet energy for bin 1 and 2 of jet energy.

(b) Energy distribution for charged and neutrals normalised to the jet energy for bin 3 and 4 of jet energy.

Figure 10.16 – a) Energy distribution for charged and neutrals normalised to the jet energy under 105 GeV . The black line represents the full simulation, the red/blue line represents SGV fast simulation. b) Energy distribution for charged and neutrals normalised to the jet energy over 105 GeV . The black line represents the full simulation, the red/blue line represents SGV fast simulation.
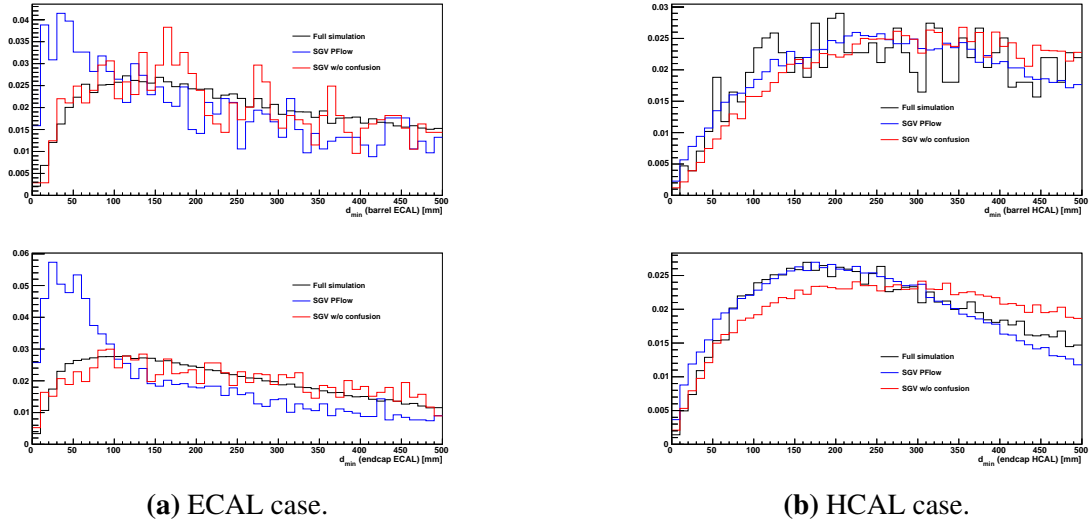
(a) ECAL case.

(b) HCAL case.

Figure 10.17 – a) Distance neutral to the closest charged distribution for the ECAL. b) Distance neutral to the closest charged distribution for the HCAL.
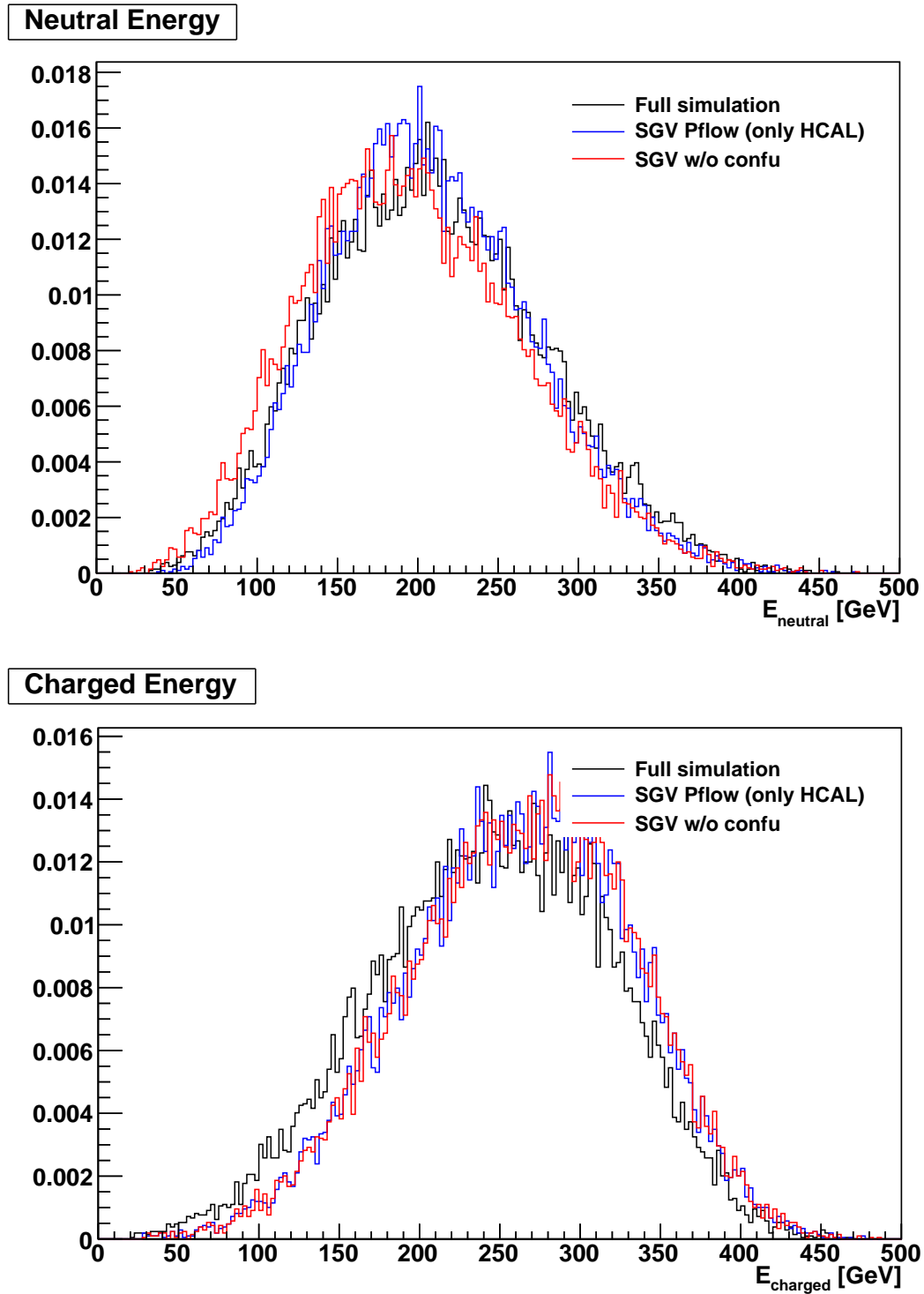
Figure 10.18 – Neutral and charged energy distributions with Particle Flow disabled for the ECAL.

10.4   Conclusion

Chapter 11

Conclusion and Outlook

References

[1] S. Agostinelli and al., "Geant4 – a simulation toolkit," *Nuclear Instruments and Methods in Physics Research Section A: Accelerators, Spectrometers, Detectors and Associated Equipment*, vol. 506, no. 3, pp. 250 – 303, 2003.

[2] H. V. P. Mora de Freitas, "Detector simulation with mokka/geant4 : Present and future," software, Laboratoire Leprince Ringuet CNRS/IN2P3 - Ecole Polytechnique 91128 Palaiseau, France, 2003.

[3] M. Frank, F. Gaede, C. Grefe, and P. Mato, "Dd4hep: A detector description toolkit for high energy physics experiments," *Journal of Physics: Conference Series*, vol. 513, no. 2, p. 022010, 2014.

[4] V. Ivanchenko and al., "Recent Improvements in Geant4 Electromagnetic Physics Models and Interfaces," in *3th Monte Carlo Conference MC2010*, vol. 2, (Tokyo, Japan), pp. 898–903, Oct. 2010.

[5] J. Apostolakis and al., "Progress in geant4 electromagnetic physics modeling and validation," in *CHEP2015*, 2015.

[6] C. Neubueser, *Comparison of Two Highly Granular Hadronic Calorimeter Concepts*. Dr., Universitat Hamburg, Hamburg, 2016. Universitat Hamburg, Diss., 2016.

[7] T. C. Collaboration, "Validation of geant4 monte carlo models with a highly granular scintillator-steel hadron calorimeter,"

[8] T. C. Collaboration, "Pion and proton showers in the calice scintillator-steel analogue hadron calorimeter," *Journal of Instrumentation*, vol. 10, no. 04, p. P04014, 2015.

[9] N. Feege, *Low-Energetic Hadron Interactions in a Highly Granular Calorimeter*. PhD thesis, Universitat Hamburg, 2011.

[10] A. Heikkinen, N. Stepanov, and J. P. Wellisch, "Bertini intra-nuclear cascade implementation in geant4,"

[11] G. Folger, V. N. Ivanchenko, and J. P. Wellisch, "The binary cascade," *The European Physical Journal A - Hadrons and Nuclei*, vol. 21, pp. 407–417, Sep 2004.

[12] G. Folger and J. P. Wellisch, "String parton models in geant4,"

[13] T. C. collaboration, "Electromagnetic response of a highly granular hadronic calorimeter," *Journal of Instrumentation*, vol. 6, no. 04, p. P04003, 2011.

[14] A. Benaglia, E. Auffray, P. Lecoq, H. Wenzel, and A. Para, "Space-time development of electromagnetic and hadronic showers and perspectives for novel calorimetric techniques," vol. 63, pp. 574–579, 04 2016.

[15] "ILCSoft web portal."

[16] F. Gaede, T. Behnke, N. Graf, and T. Johnson, "LCIO: A Persistency framework for linear collider simulation studies," *eConf*, vol. C0303241, p. TUKT001, 2003.

[17] F. Gaede, "Marlin and LCCD: Software tools for the ILC," *Nucl. Instrum. Meth.*, vol. A559, pp. 177–180, 2006.

[18] R. Fruhwirth, "Application of Kalman filtering to track and vertex fitting," *Nucl. Instrum. Meth.*, vol. A262, pp. 444–450, 1987.

[19] D. Jeans and O. Hartbrich, "Realistic calorimeter hit digitisation in the ILDCaloDigi processor," 2015.

[20] O. Hartbrich, *Scintillator Calorimeters for a Future Linear Collider Experiment*. PhD thesis, Hasylab, DESY, Hamburg, 2016.

[21] M. A. Thomson, "Particle Flow Calorimetry and the PandoraPFA Algorithm," *Nucl. Instrum. Meth.*, vol. A611, pp. 25–40, 2009.

[22] M. Berggren, "Sgv 3.0 - a fast detector simulation,"

[23] M. Pohl and H. J. Schreiber, "Simdet - version 4 a parametric monte carlo for a tesla detector,"

[24] B. Li, K. Fujii, and Y. Gao, "Kalman-filter-based track fitting in non-uniform magnetic field with segment-wise helical track model,"

[25] M. Chera, "Particle flow in sgv: Implementation and comparisons," 2014.

[26] J. S. Marshall and M. A. Thomson, "The pandora particle flow algorithm,"

[27] S. Catani, Y. Dokshitzer, M. Olsson, G. Turnock, and B. Webber, "New clustering algorithm for multijet cross sections in e+e- annihilation," *Physics Letters B*, vol. 269, no. 3, pp. 432 – 438, 1991.

[28] S. Moretti, L. Lönnblad, and T. Sjöstrand, "New and old jet clustering algorithms for electron-positron events,"

[29] F. J. Mueller, *Development of a Triple GEM Readout Module for a Time Projection Chamber & Measurement Accuracies of Hadronic Higgs Branching Fractions in ννH at a 350 GeV ILC*. Dr., Universitat Hamburg, Hamburg, 2016. Universität Hamburg, Diss., 2016.

Acknowledgments